VYSOKÉ UČENÍ TECHNICKÉ V BRNĚ

BRNO UNIVERSITY OF TECHNOLOGY

FAKULTA STROJNÍHO INŽENÝRSTVÍ

FACULTY OF MECHANICAL ENGINEERING

ENERGETICKÝ ÚSTAV

ENERGY INSTITUTE

OPTIMALIZACE DIFUZORU VODNÍ TURBÍNY S VYUŽITÍM ADJOINT ŘEŠIČE

HYDRAULIC TURBINE DIFFUSER OPTIMIZATION USING ADJOINT SOLVER

DIPLOMOVÁ PRÁCE

MASTER'S THESIS

AUTOR PRÁCE — **Bc. Jakub Pham**

AUTHOR

VEDOUCÍ PRÁCE — **doc. Ing. Pavel Rudolf, Ph.D.**

SUPERVISOR

BRNO 2024

BRNO UNIVERSITY OF TECHNOLOGY
FACULTY OF MECHANICAL ENGINEERING

Assignment of Master's Thesis

Institut:	Energy Institute
Student:	**Bc. Jakub Pham**
Degree programm:	Power and Thermofluid Engineering
Branch:	Fluid Engineering
Supervisor:	**doc. Ing. Pavel Rudolf, Ph.D.**
Academic year:	2023/24

As provided for by the Act No. 111/1998 on higher education institutions and the BUT Study and Examination Regulations, the director of the Institute hereby assigns the following topic of Master's Thesis:

Hydraulic turbine diffuser optimization using adjoint solver

Brief description:

The diffuser of a hydraulic turbine has the task of converting part of the kinetic energy leaving the impeller into pressure energy with the highest possible efficiency. For off–design operating regimes, a swirling flow enters the diffuser, which tends to create instabilities in the form of a vortex rope. The vortex rope reduces the efficiency, but above all it is a source of unwanted pressure pulsations.

Goals of the master's thesis:

The student will perform a computational shape optimization of a diffuser behind a vortex generator that mimics the impeller of a Francis turbine. The optimization will be based on the use of an adjoint solver in the ANSYS Fluent software and its main objective will be to suppress the vortex rope in off–design regimes.

Recommended bibliography:

DÖRFLER, P.; SICK, M. a COUTU, A. Flow-Induced Pulsation and Vibration in Hydroelectric Machinery. Springer, 2013.

KUMAR, S.; CERVANTES, M.J. a GANDHI, B.K. Rotating vortex rope formation and mitigation in draft tube of hydro turbines – A review from experimental perspective. Renewable and Sustainable Energy Reviews. 2021, roč. 136, s. 1-23.

OBERTA, Brian. Tvarová optimalizace sací trouby Francisovy turbíny pro potlačení vírového copu. Brno, 2023. Dostupné také z: https://www.vut.cz/studenti/zav-prace/detail/

150378. Diplomová práce. Vysoké učení technické v Brně, Fakulta strojního inženýrství, Energetický ústav. Vedoucí práce Pavel Rudolf.

Deadline for the submission of Master's Thesis is given by the Schedule of the Academic year 2023/24.

In Brno,

L. S.

doc. Ing. Jiří Pospíšil, Ph.D. Director of the Institute	doc. Ing. Jiří Hlinka, Ph.D. FME dean

Abstract

This work deals with the shape optimization of the draft tube of a swirl generator that mimics the runner of a Francis turbine. The optimization is based on the use of the adjoint solver in ANSYS Fluent. The primary objective was to suppress the vortex rope in off-design regimes. An iterative optimization methodology for the adjoint solver was established. The objective function for the adjoint solver was selected with the goal of minimizing swirl around the diffuser axis. A new diffuser design was presented and analyzed, after which a comparison was made between vortex rope behaviour and flow field characteristics inside the new and old diffuser designs. It was found that shape optimization had not resulted in any significant improvement in vortex rope behaviour, with the energy of the vortex rope being only transferred further away from the hub of the swirl generator. Recommendations for future methods of vortex rope mitigation were made at the conclusion of this work.

Keywords

vortex rope, shape optimization, adjoint method, CFD, draft tube, diffuser

Rozšířený abstrakt

S rostoucí globální poptávkou po elektrické energii a snahou o snižování uhlíkových emisí se stává nezbytným posilování role obnovitelných zdrojů energie. Solární a větrné elektrárny představují významnou část tohoto přechodu, avšak jejich výkonnost je značně ovlivněna klimatickými podmínkami a střídáním dne a noci, což vede k jejich inherentní nestabilitě. Vodní elektrárny přitom nabízejí rychlou odezvu a stabilitu, což je činí důležitými prvky v současném energetickém mixu. Aby mohly efektivně reagovat na proměnlivou poptávku, je nezbytné, aby byly schopny provozu v širokém rozsahu podmínek. Tento požadavek na flexibilitu však přináší nové výzvy, zejména v podobě hydrodynamických nestabilit, které vznikají při provozu mimo optimální podmínky.

Jednou z hlavních nestabilit, která se v těchto situacích vyskytuje, je vírový cop, který vzniká v difuzoru za oběžným kolem turbíny. Tento fenomén má negativní dopady, jako jsou tlakové pulzace, nadměrný hluk, vibrace a zkrácení životnosti klíčových komponent. Proto je nezbytné hledat způsoby, jak tyto vírové struktury potlačit a tím rozšířit provozní rozsah turbín. Různé metody, jako je přidání žeber, prodloužení náboje oběžného kola, drážky nebo vstřikování vzduchu a vody, byly otestovány s cílem zmírnit tyto negativní jevy, avšak s omezeným úspěchem.

Tato diplomová práce se zaměřuje na tvarovou optimalizaci difuzoru za účelem potlačení vírového copu v mimooptimálních podmínkách pomocí adjungovaného řešiče v ANSYS Fluent. V první kapitole je podána studie mechanismu a chování vírového copu ve vodních turbínách, stejně jako přehled různých metod pro jeho zmírnění. Dále jsou prozkoumány simulace pomocí výpočtového modelování proudění (CFD), které identifikují vhodné turbulentní modely pro předpověď vírových copů, přičemž pokročilejší modely jako RSM (Reynolds Stress Model) nebo LES (Large Eddy Simulation) se ukazují jako nejspolehlivější. Druhá kapitola je věnována adjungované metodě, která je efektivním matematickým nástrojem pro výpočet gradientů (citlivostí) u velkého počtu proměnných, což ji činí vhodnou pro úlohy tvarové optimalizace, kde jsou proměnnými souřadnice uzlů výpočtové sítě. Jsou zde formulovány základní rovnice adjungované metody a její aplikace v CFD simulacích, kde se prosadila především v automobilovém a leteckém průmyslu. Byla zde představena metodologie iterativního procesu návrhu nového tvaru difuzoru.

Následující kapitoly představují testovací případ s jednoduchou geometrií, který ilustruje základní principy tvarové optimalizace pomocí adjungované metody. Tento krok je klíčový pro pochopení možností a omezení adjungovaného řešiče v ANSYS Fluent. Dále je uvedena výpočtová síť, okrajové podmínky a nastavení adjungovaného řešiče. V tomto případě bylo sledováno odtrhávání Kármánových vírů za válcem s cílem minimalizovat odporový součinitel válce. Optimalizace ukázala, že adjungovaný řešič může být efektivní, když se podařilo snížit cílovou funkci o 63 % pomocí změny tvaru válce.

Hlavní část práce se zaměřuje na tvarovou optimalizaci difuzoru za použití trojrozměrných, nestacionárních CFD simulací vírového copu. Pro zajištění přesných výsledků byla vytvořena strukturovaná síť a zvolen model turbulence RSM. Cílovou funkcí pro adjungovaný řešič byl moment hybnosti proudění kolem osy difuzoru, který se měl minimalizovat. Závěrečné výsledky ukazují, že optimalizovaný tvar difuzoru, který vznikl jako zvonovitý s úzkou částí na vstupu a širší částí na výstupu, dokázal částečně snížit moment hybnosti proudění kolem osy difuzoru. Cílová funkce se snížila o 18 %, což naznačuje částečný úspěch, avšak energie vírového copu byla pouze přesunuta dál od náboje, cop nebyl potlačen. Oblast zpětného toku se rovněž vzdálila od náboje bez výrazné změny své velikosti. Vlivem zúžení difuzoru a tedy zmenšení příčných průřezů se zvýšila axiální rychlost uvnitř difuzoru. Tlakové pulzace se dokonce zvýšily důsledkem tvarové optimalizace difuzoru.

Celkově výsledky ukazují, že tvarová optimalizace difuzoru nepřinesla očekávané potlačení vírového copu. Výzkum naznačuje, že samotný tvar difuzoru má na chování vírového copu minimální vliv. Efektivnější metodou se ukazuje manipulace rychlostního pole, např. rychlostního trojúhelníku na výstupu z oběžného kola, což je přístup používaný například u Kaplanových turbín s nastavitelnými lopatkami. Pro Francisovy turbíny je vhodné zvážit aktivní metody, jako je vstřikování kapaliny do systému. Tato diplomová práce přináší důležité poznatky pro oblast optimalizace vodních turbín a nabízí směr pro budoucí výzkum, který by mohl vést k efektivnějším metodám potlačování vírového copu a zlepšení provozních vlastností vodních elektráren.

Bibliographic citation

PHAM, Jakub. Hydraulic turbine diffuser optimization using adjoint solver [online]. Brno, 2024 [cit. 2024-05-24].

Also available at: https://www.vut.cz/studenti/zav-prace/detail/158156. Master's thesis. Brno University of Technology, Faculty of Mechanical Engineering, Energy Institute. Supervisor Pavel Rudolf.

Declaration

I hereby declare that the thesis submitted is my own unaided work. All sources used are acknowledged as references.

Bc. Jakub Pham, B.Sc.

Acknowledgements

I would like to express my gratitude to my parents for their unwavering support, which allowed me to concentrate fully on my studies. I would also like to thank my long-time girlfriend for her support and motivation that kept me going throughout the years. I am grateful to my supervisor doc. Ing. Pavel Rudolf, Ph.D. that originally fueled my motivation for fluid dynamics and computational modelling and I would like to thank him for his approach to students and guidance. My thanks also goes to Ing. David Štefan, Ph.D. and Ing. Roman Klas, Ph.D. for their invaluable contributions and assistance with the thesis.

Contents

Introduction

As the demand for electricity increases in line with demographic growth, so too does the necessity to reduce emissions from carbon sources. Renewable sources, such as solar and wind power plants, are the primary drivers of this transformation. However, their output is significantly influenced by weather conditions, rendering them inherently unstable as a source of energy. To mitigate this instability, quick-to-response, on-demand energy sources are required. In this regard, hydroelectric power meets both of these requirements. Consequently, the role of hydropower is becoming increasingly prominent in today's energy mix. In order to accommodate the demand, hydropower plants must be capable of functioning in a wide range of operational conditions. However, this flexibility comes at a cost, as water turbines are designed for a specific operating condition. When operating in off-design conditions, various hydrodynamic instabilities are generated within the water turbine and the draft tube. These instabilities have a negative impact on the turbine through the generation of pressure pulsations, excessive noise, and vibrations, as well as shortening the lifetime of exposed parts. It is therefore necessary to mitigate these instabilities and reach the widest possible operating range.

One of the vortex structures generated in the draft tube during off-design conditions is the vortex rope. This is a region of low pressure rotating inside a draft tube, which usually takes the form of a helix. Various methods have been tested to mitigate this phenomenon, including the addition of fins into the draft tube, runner cone extensions, grooves, or air and water injection. This thesis will deal with the shape optimization of the draft tube with the goal of suppressing the vortex rope in off-design conditions. The first chapter will give a brief study of the vortex rope in water turbines, its mechanism and behaviour. A variety of mitigation methods for the vortex rope will be presented. Computational fluid dynamics (CFD) simulations of the vortex rope will be explored, demonstrating which turbulent models are most suitable for this task. The second chapter will introduce the adjoint method, explaining why this mathematical method is well suited for shape optimization. The fundamental equations of the adjoint method will be formulated, and a link to its use in CFD simulations will be shown.

The following chapter presents a test case with simple geometry, which serves to illustrate the fundamental principles of the adjoint shape optimization process. The objective was to test the capabilities and limitations of the adjoint solver in ANSYS Fluent. The final two chapters address the primary focus of the thesis, namely the shape optimization of the draft tube. The computational mesh and boundary conditions are presented, along with a detailed description of the adjoint solver setup, including the objective function. Finally, the optimized shape of the draft tube is presented, and the flow field is analyzed in detail in order to understand how the vortex rope reacted to the changed shape of the draft tube.

Chapter 1

Vortex rope in water turbines

Due to the variable demand of the electricity market, today's hydroelectric turbines are increasingly subjected to load ramping, quick start-stop, emergency shutdowns, and operation in off-design conditions. These actions are intended to minimize frequency oscillations in the power grid; however, they negatively affect the lifespan of a turbine, causing, e.g., intense vibrations, pressure pulsations, and even failure of the machine components[1].

In particular, when operating at part load conditions, single-regulated turbines such as Francis turbines show a strong swirl at the runner exit. This phenomenon can be attributed to the mismatch between the angular momentum produced by the guide vanes and that consumed by the runner. The excess swirl then enters the turbine draft tube as an additional tangential component of the absolute velocity v_u. Compared to the Kaplan turbine, which can partially control the flow field through its adjustable runner blades and mitigate the adverse effects of the swirl, the Francis turbine with its fixed blades is at a disadvantage and experiences more negative effects in off-design conditions[2]. The frequent transients and off-design conditions, both part load (PL) and high load (HL) result in flow instabilities in the draft tube[1].

The draft tube is an essential part of a reaction turbine for high efficiency. The primary function is the conversion of the excessive kinetic energy into useful static pressure. The velocity triangles at the draft tube inlet, as seen in Fig. 1.1, illustrate the effect of the varying flow rates on the draft tube flow field.

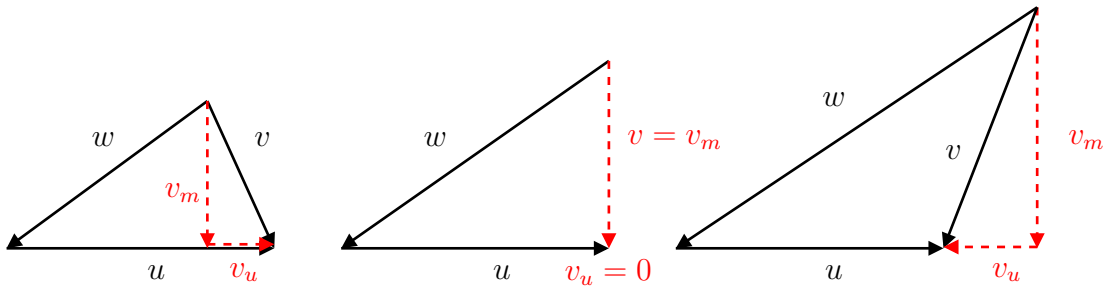

Figure 1.1: Velocity triangles at the draft tube inlet; u is the circumferential velocity; w is the relative velocity; v_m and v_u are the axial and tangential components of the absolute velocity v, left: part load, middle: BEP, right: high load

The best efficiency point (BEP), shown as the middle triangle in the figure, represents

the theoretical best-case scenario with purely axial outlet velocity v and no swirl or tangential velocity component v_u. However, in real operation, some residual swirl is maintained to allow higher draft tube opening angles to be achieved without boundary layer separation[3]. The flow at both PL and HL conditions, in contrast to the best efficiency point, exits the runner at a suboptimal angle, leading to a significant tangential velocity component.

At PL conditions, characterized by a reduced flow rate compared to BEP, the tangential velocity component v_u increases. This increase is dictated by the fixed relative angle between u and w and the runner speed. The former is determined by the blade shape, and the latter by the frequency in the electric grid. Consequently, the direction of the tangential velocity vector v_u aligns with the runner rotation, causing the water to rotate in the same direction as the runner. At HL conditions, where the flow rate is higher than that at BEP, the tangential velocity vector points in the opposite direction than the runner rotation, meaning that the water in this case rotates in the opposite direction to the runner[1].

1.1 Vortex breakdown

The flow at PL and HL conditions shows excessive swirl, which increases its vulnerability to instabilities. Specifically, at PL, the instability takes the form of a spiral vortex resulting from a phenomenon known as vortex breakdown. The vortex rope formation has been shown to be closely related to the vortex breakdown[1,3]. Rudolf et al.[2] defined vortex breakdown as "a sudden change of the flow structure at critical swirl level."

Numerous theories exist that aim to explain vortex breakdown and its formation; however, there is currently no overarching theory describing all of its characteristics. One of the theories involves the idea of hydrodynamic instabilities. It states that if local stagnation occurs in the decelerated axial flow, then vortex breakdown occurs. Rudolf et al.[2] characterize the vortex breakdown formation as a result of "flow deceleration in the vicinity of the axis, the formation of a stagnation point, and the onset of a re-circulation bubble, eventually resulting in vortices being rolled up through the Kelvin-Helmholtz instability along the shear layer between the two opposing streams." Additional information can be found in the works of Leibovich[4,5] and Sarpkaya[6].

Several vortex breakdown types have been identified depending on the swirl strength and the Reynolds number. In the case of diverging tube flows, three types of vortex breakdown have been observed[4,5,6], namely: (a) double helix spiral type, (b) spiral type, and (c) bubble type.

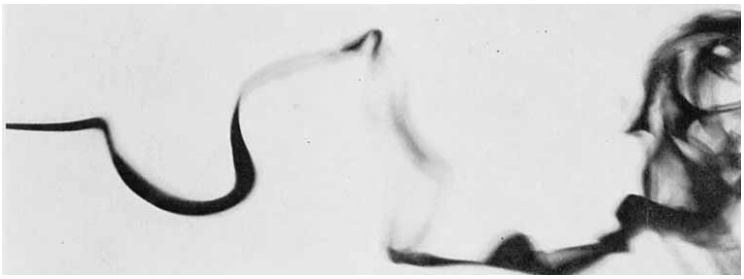

Figure 1.2: Spiral vortex breakdown, photographed by Sarpkaya[6]

The spiral type is the one occurring in the draft tube of hydro turbines[1]. The

phenomenon takes place when the flow decelerates rapidly along the axis of the vortex core before suddenly transforming into a spiral configuration, as shown in Fig. 1.2. Here, the water in the central region loses its kinetic energy to move downstream against the pressure gradient, leading to a stagnation point forming along the axis. A vortex sheet may form between the central stalled region and the main flow with the surrounding vortex[7]. The sheet of vortex filaments can easily be rolled up into a single vortex, which rotates with the main flow in the draft tube, as shown in Fig. 1.3. The pitch of the spiral vortex rope depends on the strength of the swirl. If the main swirling flow rotates in a clockwise direction, the tail of the spiral vortex core will rotate counter-clockwise[1].

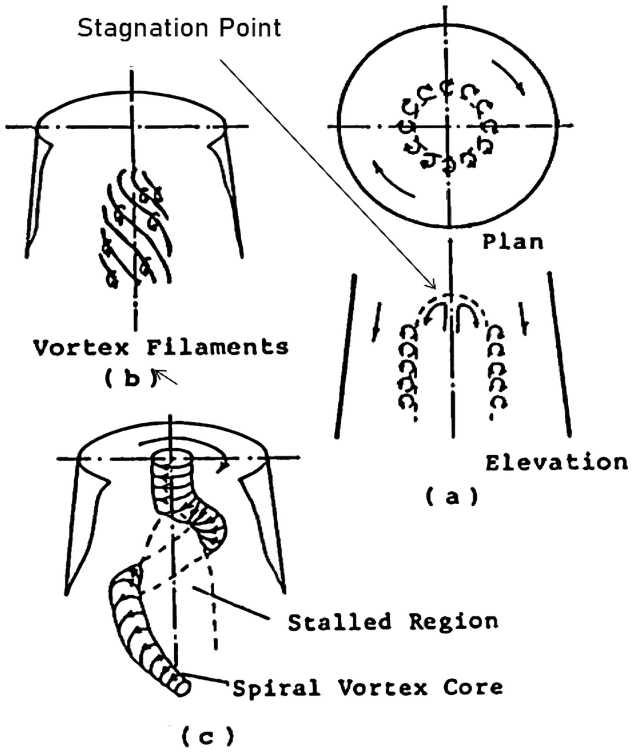

Figure 1.3: Origin of the spiral vortex rope in the draft tube, sketched by Nishi[7]

1.2 Characteristics of the vortex rope

One of the main parameters determining the shape and behaviour of the vortex rope in the draft tube is the swirl rate m. The swirl rate is defined as the ratio of the flux of angular momentum to the flux of axial momentum[1,8],

$$m = \frac{\int_0^R v_m \, v_u \, r^2 \, dr}{R \int_0^R v_m^2 \, r \, dr} \tag{1.1}$$

where r is the radial distance and R is the radius of the draft tube.

Another important parameter is the swirl angle ϕ at the exit of the runner outlet, which is defined as:

$$\phi = \arctan \frac{v_u}{v_m} \tag{1.2}$$

The swirl angle is a crucial factor for highly swirling flow, as a greater angle results in a stronger swirl. The velocity distribution in the Francis turbine's draft tube is dependent on both the strength of the swirl and the characteristic Reynolds number. Once a specific condition is met, the kinetic energy of the main axial flow is insufficient to overcome the adverse pressure gradient present in the draft tube. Initially, a region of stagnation develops at the center of the draft tube, followed by the reversal of fluid flow inside that stagnation region. The adverse pressure gradient and opening angle of the draft tube cone play a crucial role in this phenomenon[1]. An increased opening angle of the draft tube cone results in a greater adverse pressure gradient, and therefore a lower swirl is required for the formation of the vortex rope. According to Sarpkaya[6], a 20 % lower swirl was required for vortex formation in a divergent duct compared to the parallel duct employed in experiments by Harvey[9].

Nishi et al.[7] identified four flow regimes in an elbow draft tube based on the vortical structures using the swirl rate m and the cavitation number K. These regimes are depicted in Figure 1.4. The cavitation number characterizes the cavitation condition in the draft tube and is defined as:

$$K = \frac{2g \cdot \mathrm{NPSH} \cdot \pi^2 R^4}{Q^2} \tag{1.3}$$

where NPSH is the net positive suction head and Q is the volumetric flow rate.

Regime I: The vortex rope appears almost straight, and no backflow region is observed in the straight portion of the draft tube upstream of the elbow.

Regime II: It features an unstable vortex rope that assumes varied forms irregularly.

Regime III: A stable, single vortex rope is observed, with the stagnation point located near the diffuser inlet.

Regime IV: Twin or occasionally triple vortex ropes are observed, with the stagnation point reaching the runner hub tip.

The presence of a rotating vortex rope in the Francis turbine's draft tube is associated with several adverse effects, including pressure pulsations, power swings, noise, and vibration. Off-design conditions cause a decrease in efficiency, mostly due to poor pressure recovery caused by the vortex rope and other instabilities. Typically, pressure measurements at the cone wall of the draft tube are used to detect the existence of a vortex rope. The pressure pulsations are regularly occurring under PL conditions. This pulsation is approximately periodic, the period of the pressure pulsation is the same as that for the rotation (precession) of the corkscrew, which may be observed visually during an experiment[10]. Rheingans[11] observed the relative frequency of precession at a value of approximately 1/3.6 of the runner frequency. The connection between the guide vane opening and the pressure amplitude and swirl intensity was significant[1]. Francis turbines encountered intense draft tube surge, resulting in significant structural vibrations at PL conditions[12].

In addition to the effects of the vortex rope, other mechanical effects are noticeable during longer operating periods under PL conditions. The runner of the Francis turbine undergoes intense stress and dynamic loading when continuously running under such

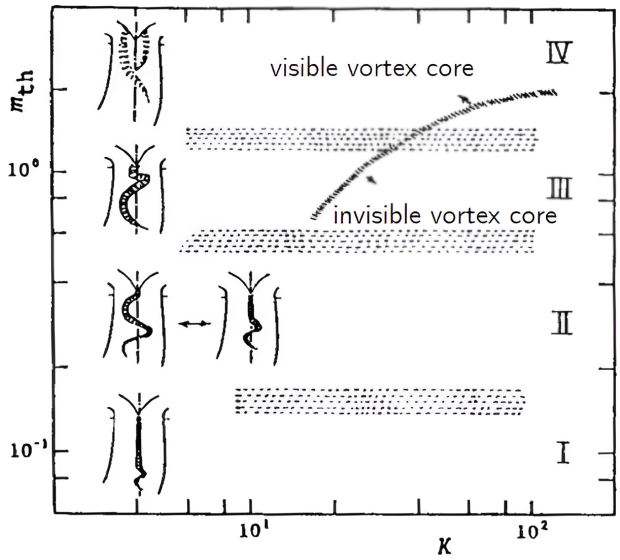

Figure 1.4: Vortex rope flow regimes in an elbow draft tube depicting different vortex rope structures, by Nishi et al.[7]

conditions[1,13]. The helical vortex rope at PL conditions produces rotating radial forces and bending torque, which cause radial vibrations[13].

To address these effects of the rotating vortex rope, several mitigation methods have been developed in the past decades. These can be classified into two categories: (a) geometrical methods and (b) fluid methods[1]. Geometrical methods are classified as passive as they do not operate in an active feedback loop to regulate the flow in the draft tube or the geometry and include fins, J-grooves, and shaft/cone extensions. Fluid methods include water and air injection. All these methods have been found to be only partially effective in mitigating the effects of the rotating vortex rope. In most cases, the mitigation of one effect leads to the amplification of another negative effect. Further optimization is required for practical implementation[1]. The Fig. 1.5 shows a runner cone extension in a draft tube. This photo is courtesy of Vekve[14].

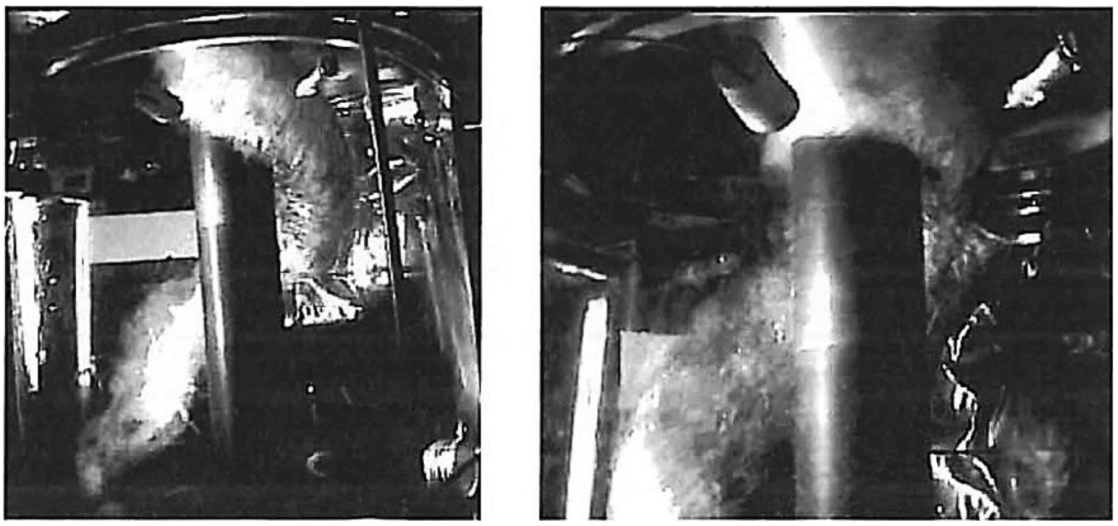

Figure 1.5: Runner cone extension, photographed by Vekve[14]

1.3 CFD simulations of the vortex rope

Over the past few decades, there has been significant research on the vortex rope and how to mitigate its effects. Scientists have used various numerical models to simulate the vortex rope in a draft tube, both at PL and HL conditions. The initial simulations involved a two-equation turbulence model, specifically the standard k-ϵ model by Launder and Spalding[15]. Vu et al.[16] employed this model to predict flow behaviour in the draft tube and energy loss in hydraulic turbine components. Similarly, Resiga et al.[17] used the same model to investigate the effects of an axial hub jet on the pressure fluctuations caused by the draft tube vortex rope. Ruprecht et al.[18] have discussed the importance of turbulence models in accurately capturing the effects of the vortex rope and conclude that the standard k–ε model is unable to predict the vortex rope due to excessive damping.

Furthermore, the computational grid is of major importance for a realistic prediction of the vortex and the related pressure drop towards the vortex core. If certain criteria are not met, both the velocity gradients and the pressure drop will be under-predicted[10].

Yaras and Grosvenor[19] used both Menter's two-equation shear stress transport (SST) model[20] and Spalart's one-equation eddy-viscosity model[21] to simulate swirling flows. Their study suggests that both models are unsuitable for accurately modelling strongly swirling, confined flows.

The limitations of two-equation models, which are commonly used due to their lower computational expense, prompted experimentation with more sophisticated turbulence models. The latter proved effective in accurately representing the shape and movement of the vortex rope. Such models include the Reynolds stress model (RSM) and scale resolving models such as the large-eddy simulation (LES), the detached-eddy simulation (DES), or the stress-blended eddy simulation (SBES), which require more refined grids and relatively longer computation times.

Rudolf et al.[2] utilised RSM implemented in the commercial software ANSYS Fluent to simulate the flow in a diffuser of a swirl generator. The aim of the study was to manipulate the swirling flow instability to mitigate pressure pulsations caused by the vortex rope. Experimental testing was carried out using a Francis turbine model, comparing three water injection methods: full circular jet, annular jet with opposite swirl, and annular jet with a 5 mm gap. The results showed that the best results, in terms of reduction of static pressure pulsations, were achieved with the original full circular jet. The simulations showed that the resulting vortex rope shape was similar to that observed during experimental testing, and the dominant frequency associated with vortex rope rotation was very close to the experimental one. However, the amplitude of the first harmonic was underestimated by 20 %.

Minakov et al.[22] conducted a comparative study of flow simulations in a laboratory model of a Francis turbine under three different conditions: part load, BEP, and high load. The researchers employed various turbulence models, including two eddy-viscosity models (realizable k-ε, k-ω SST), a Reynolds stress model, detached-eddy simulation, and large-eddy simulation. The results indicated that the k-ω SST model is too dissipative, whereas RSM predicts a vortex rope with a similar rough shape to more detailed DES and LES simulations. However, RSM is unable to capture the tendency of the vortex rope to break into two intertwined structures (see Fig. 1.6).

Rajan and Cimbala[23] modelled the vortex rope using the DES turbulence model,

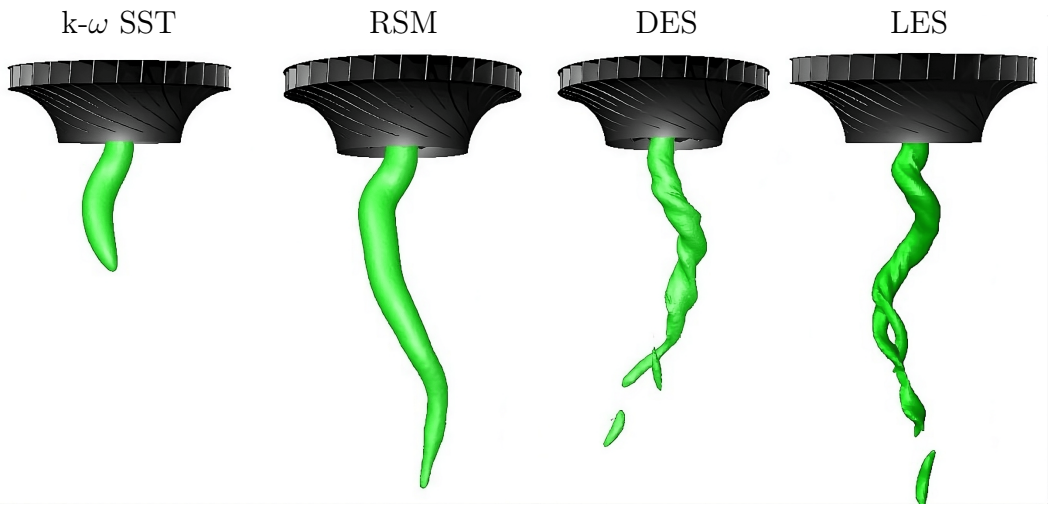

Figure 1.6: Comparison of vortex rope shapes, identified by pressure isosurfaces, in the PL regime simulated using different turbulence models, by Minakov et al.[22]

alongside the realizable k-ε model using ANSYS Fluent. The authors presented the vortex rope at four different operating points (refer to Fig. 1.7). A qualitative analysis indicates that, as the flow rate reduces, the size of the vortex rope increases. At the BEP (far right), the rope is thin and confined to a limited area surrounding the axis of the draft tube, whereas the vortex rope at 91 % of BEP (far left) spreads out into the radial and axial directions and occupies a greater portion of the draft tube.

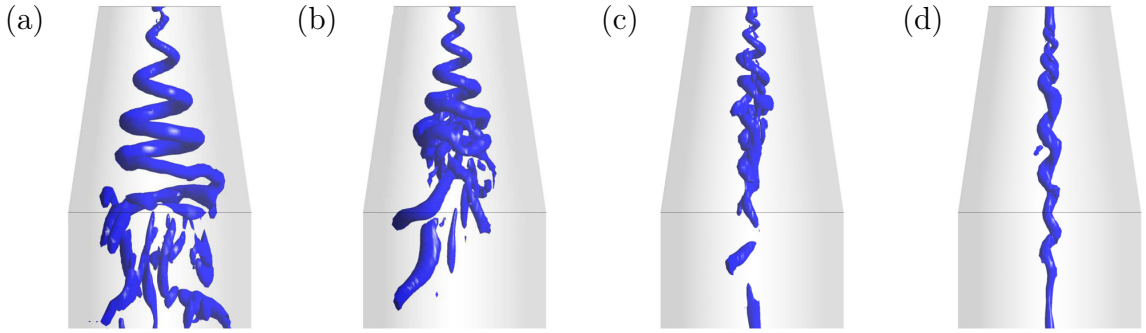

Figure 1.7: Visualisation of the vortex rope at four different conditions with flow rate increasing from the left to right; (a) 91 % of BEP, (d) BEP, by Rajan and Cimbala[23]

Urban[3] conducted a study on the behaviour of swirling flows in a self-designed swirl generator using two different turbulence models: the SBES model and RSM. The main objective was to investigate the effectiveness of various control methods in reducing the damage caused by vortex ropes in water turbines, one of which incorporated injecting a water jet into the flow to counteract the formation of the vortex rope.

The results of the simulations showed that the RSM and SBES model can reasonably predict the behaviour of the swirling flow in the water turbine. It was also shown that injecting a water jet into the flow can significantly reduce the effect of the vortex rope. The effectiveness of the method depends on the flow rate of the water jet and the injection point location.

Junginger and Riedelbauch[24] conducted a study of flow simulation in a full load propeller turbine using the scale adaptive simulation (SAS) and the stress-blended eddy simulation turbulence models. The data revealed that SAS resolves fewer eddies in comparison to SBES. Furthermore, SBES accurately predicted all key integral parameters.

It should be pointed out that all the work presented here assumed a single-phase flow. However, in reality, cavitation frequently occurs inside the vortex rope, significantly affecting its shape and behaviour.

Flemming et al.[25] simulated cavitating vortex ropes in a hydraulic turbine. Two different numerical approaches were compared: a single-phase method and a two-phase method with a cavitation model. The ANSYS CFX software was employed using the SST model. The results of the simulations showed that both calculation methodologies produced vortex ropes, but with significant differences in size, shape, and location. The single-phase approach predicted a larger vortex rope with attachment closer to the runner blades on the hub, while the two-phase approach had a smaller vortex rope that extended further into the draft tube elbow. The two-phase approach provided more detailed surface contours and was consistent with model observations.

In summary, this chapter has examined the complex phenomenon of vortex ropes in hydraulic turbines, with a particular focus on their behaviour in off-design scenarios. The study of vortex breakdown and its correlation with the spiral vortex rope highlighted the importance of understanding the mechanisms of these flow structures. Critical parameters, including swirl rate and swirl angle, were identified for characterizing vortex ropes, with distinctions drawn between different flow regimes in the draft tube.

Furthermore, the detrimental effects of vortex ropes, such as pressure pulsations and structural vibrations, underlined the critical need for effective mitigation strategies. CFD simulations, employing various turbulence models, proved to be important in understanding and predicting vortex rope behaviour. It was essential to acknowledge the limitations of existing numerical models. This work laid the foundation for future research efforts aimed at refining the understanding of vortex ropes and advancing strategies for their efficient mitigation in practical hydraulic turbine applications.

To conclude this chapter, the subsequent work will concentrate solely on the single-phase flow simulation of the vortex rope, considering limitations in time and practicality. Validation of the predicted draft tube pressure pulsation against experimental data obtained in a model test shows that single-phase flow simulations give very good results for both the frequency and the amplitude of the pressure pulsations[10]. The RSM model was selected as the turbulence model of choice due to its accuracy for highly swirling flows and computational efficiency.

The following chapter outlines the second main part of this thesis, which covers the method for the shape optimization of the draft tube known as the adjoint method.

Chapter 2

Adjoint method

Developing a part with an optimal design is a complex task. In most cases, it requires consideration of numerous design variables. However, manually changing these variables through trial and error is costly and unlikely to result in the optimal design. To simplify design exploration, numerical optimization can automatically find the set of design variables that minimizes a given objective function subject to design constraints. Currently, gradient-based optimization algorithms are the only practical way of dealing with optimization problems involving large numbers of variables[26].

In order to fully benefit from gradient-based optimization algorithms, it is essential to accurately and efficiently compute the derivatives of the objective and constraint functions with respect to the design variables. The use of finite differences is the simplest approach to automatically computing the necessary gradients directly from the partial derivative definition. Nonetheless, finite difference approximations are susceptible to numerical errors and are inefficient because their cost is proportional to the number of design variables[26,27].

Adjoint-based optimization, which was developed by Lions and Pironneau[28,29] in the 1970s and pioneered by Jameson[30] in the 1980s, has been acknowledged as an effective method for tasks involving multiple design variables. Further information on the historical development of the adjoint method can be found in these papers[26,27,31]. The adjoint method's underlying principle enables an elegant implicit calculation of sensitivities, i.e., the derivative of the objective function with respect to the design variables. The computational effort is independent of the number of design variables and requires only one solve of the adjoint counterparts of the governing equation system, in our case the Navier-Stokes equations[32]. When applied to a surface mesh representation of the part to be optimized, it is possible to generate information, referred to as "sensitivity maps," like the one shown in Fig. 2.1[32].

A sensitivity map tells us, for each individual surface node, how the objective function changes with respect to an infinitesimally small normal displacement of that surface node. Sensitivity maps provide information on where and how to change the geometry — perturb the surface inwards or outwards — in order to improve the objective function.

In Fig. 2.1, the red areas indicate that shifting away from the fluid — inward for the car, outward for the pipe — can improve the cost function. On the contrary, the blue sections show the areas where a surface perturbation towards the fluid would improve the performance, while changes in the greenish sections of the surface would have little

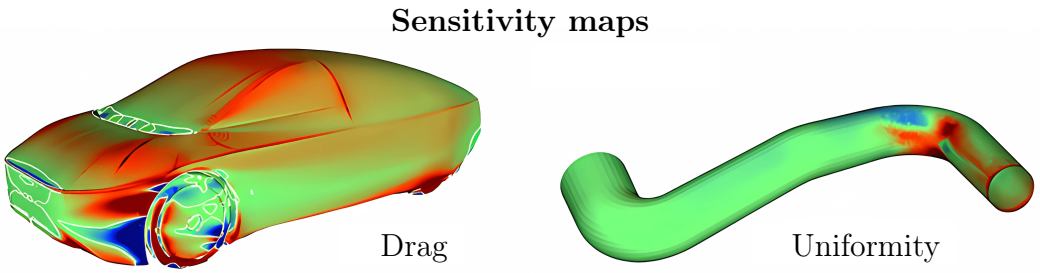

Figure 2.1: Sensitivity maps for different objective function — drag on the left and the flow uniformity on the right, by Othmer[32] (edited)

effect on the cost function. The white lines on the car body represent the isolines of zero sensitivity[32].

There are two fundamental approaches to formulating the adjoint for a set of partial differential equations (PDEs): the continuous approach and the discrete approach[26,27,31]. The diagram in Fig. 2.2 illustrates the difference between the two approaches. In both cases, one ends up with a set of discrete adjoint equations. The continuous approach involves differentiating the PDEs analytically to derive the continuous adjoint equations, which are then discretized so that they can be solved numerically. In contrast, the discrete approach starts with the discretized form of the PDEs, which is then linearized to obtain the discrete adjoint equations[26,31].

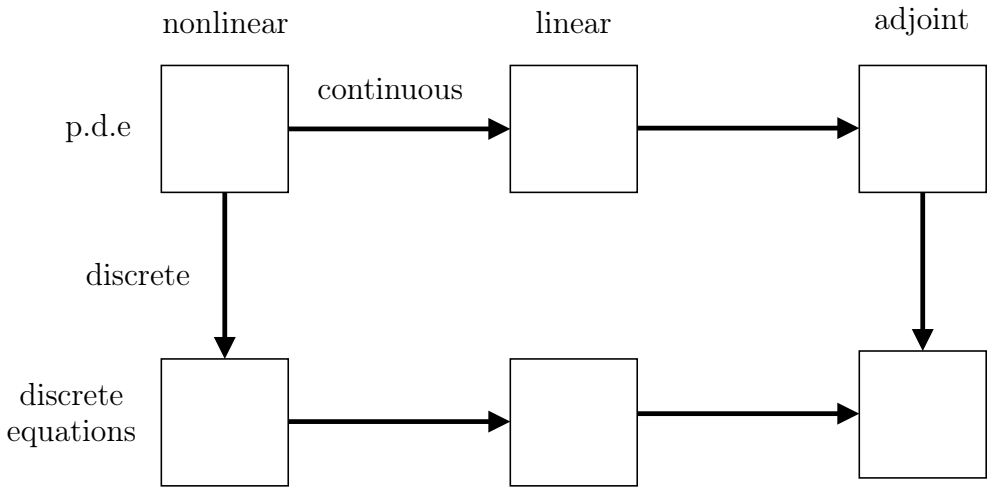

Figure 2.2: Alternative approaches to forming discrete adjoint equations, by Giles et al.[31] (edited)

The continuous approach has certain drawbacks, including low precision for coarser meshes and challenging implementation. Additionally, the initial linearization of PDEs and their subsequent discretization mean that the discretized form of these equations is only guaranteed to give a fully consistent gradient in the limit of an infinitely fine mesh. The continuous adjoint system can produce inaccurate gradients when the solution accuracy is affected by the mesh or the numerical methods[26].

Furthermore, some terms in the PDEs need to be hand differentiated, making it challenging to use the continuous adjoint system. Adjoint developers often simplify some

of the terms in the turbulence model for turbulent RANS equations, which introduces an additional source of error[26].

According to ANSYS, Inc.[33], the continuous adjoint solver offers the advantage of being largely separate from the original flow solver. The only aspect they share is that they are based on the Navier-Stokes equations. The process of discretizing and solving the partial differential equations in each scenario could, in principle, differ significantly. Although the flexibility may be attractive, it can also be the downfall of the approach. Inconsistencies in modelling, discretization, and solution approaches have the potential to significantly degrade the sensitivity information, especially for problems involving wall functions and complex engineering configurations.

The discrete adjoint method has been the primary focus of recent research on adjoints. This approach has the advantage that it provides numerically consistent derivatives, independent of the coarseness of the grid, because it is formulated from the discretized flow equations. Additionally, the partial derivatives appearing in the discretized adjoint equations do not require hand differentiation and can be computed using several numerical methods (e.g. finite differences). The application of these techniques enables the generation of accurate numerical derivatives, even in the case of intricate procedures such as the implementation of various turbulence models within RANS analysis. However, the major drawback of the discrete approach lies in its significantly high computational and memory expenses incurred during the calculation and storage of the exact Jacobian, which will be further explained below[26]. The ANSYS Fluent adjoint solver uses the discrete adjoint approach[33].

2.1 Formulation of the adjoint method

The derivation of the adjoint equations was adopted from the articles by Kenway[26] and Han[34], with modifications made for clarity.

The goal of the adjoint method is to calculate the change of the function of interest with respect to the design variables. This can be expressed as the total derivative $df/d\boldsymbol{x}$, where f is the function of interest (e.g. drag, lift, or pressure drop) and $\boldsymbol{x}$ is the vector of design variables (e.g. surface shape). The discrete adjoint method assumes that a discretized form of the governing equations is solved for the state variable vector $\boldsymbol{w}$ (in our case, the flow variables). Within each cell, the flow variables include pressure and velocity, as well as, for example, k and ω for a turbulence model. After reaching convergence, a discrete set of governing equations is satisfied, which mirrors the modelled flow physics. This can be represented as

$$\boldsymbol{R}\left(\boldsymbol{x},\boldsymbol{w}\right) = 0 \tag{2.1}$$

where $\boldsymbol{R}$ is the vector of residuals for the governing equations. The function of interest is then a function of both the design variables and the state variables, i.e.

$$f = f(\boldsymbol{x},\boldsymbol{w}) \tag{2.2}$$

In general, there may be multiple functions of interest, such as velocities in multiple directions or design constraints. However, we will assume the function of interest is a scalar without loss of generality. For each additional function of interest, another

adjoint system must be solved. To calculate the total derivative $df/d\boldsymbol{x}$, the chain rule is applied:

$$\frac{df}{d\mathbf{x}} = \frac{\partial f}{\partial \mathbf{x}} + \frac{\partial f}{\partial \mathbf{w}} \frac{d\boldsymbol{w}}{d\mathbf{x}} \tag{2.3}$$

The terms $\partial f/\partial \mathbf{x}$ and $\partial f/\partial \mathbf{w}$ can be calculated explicitly from the governing equations, making their calculation straightforward. However, the total derivative $d\boldsymbol{w}/d\boldsymbol{x}$ can only be determined implicitly, meaning the variation in the flow field depends upon the adjustment that is made to the inputs.

To solve for $d\boldsymbol{w}/d\boldsymbol{x}$, we apply the chain rule to $\boldsymbol{R}$, then use the fact that the total derivative $d\boldsymbol{R}/d\boldsymbol{x}$ must equal zero to ensure the governing equations remain feasible with respect to variations of the design variables. We can express this as follows:

$$\frac{d\mathbf{R}}{d\mathbf{x}} = \frac{\partial \mathbf{R}}{\partial \mathbf{x}} + \frac{\partial \mathbf{R}}{\partial \mathbf{w}} \cdot \frac{d\boldsymbol{w}}{d\mathbf{x}} = 0 \tag{2.4}$$

We can rearrange this to obtain the following expression for $d\boldsymbol{w}/d\mathbf{x}$.

$$\frac{d\boldsymbol{w}}{d\mathbf{x}} = -\frac{\partial \mathbf{R}}{\partial \mathbf{w}}^{-1} \frac{\partial \mathbf{R}}{\partial \mathbf{x}} \tag{2.5}$$

This term can then be substituted back into Eq. 2.4 to derive a new expression for the total derivative $df/d\boldsymbol{x}$.

$$\frac{df}{d\mathbf{x}} = \frac{\partial f}{\partial \mathbf{x}} - \overbrace{\frac{\partial f}{\partial \mathbf{w}} \frac{\partial \mathbf{R}}{\partial \mathbf{w}}^{-1}}^{\psi^T} \frac{\partial \mathbf{R}}{\partial \mathbf{x}} \tag{2.6}$$

Typically, we do not find the inverse of the Jacobian $\partial \mathbf{R}/\partial \mathbf{w}$ explicitly. Instead, the corresponding linear system is solved with the transposed Jacobian $[\partial \mathbf{R}/\partial \mathbf{w}]^T$ as the right-hand side, which yields the *adjoint equations*

$$\frac{\partial \mathbf{R}}{\partial \mathbf{w}}^T \psi = \frac{\partial f}{\partial \mathbf{w}}^T \tag{2.7}$$

where ψ is the *adjoint vector*. Much of the computational effort in an adjoint solver is in the construction and solution of this system[34]. The adjoint vector is then substituted back into Eq. 2.6 to finally calculate the total derivative.

$$\frac{df}{d\mathbf{x}} = \frac{\partial f}{\partial \mathbf{x}} - \psi^T \frac{\partial \mathbf{R}}{\partial \mathbf{x}} \tag{2.8}$$

Since the design variable $\boldsymbol{x}$ does not appear explicitly in Eq. 2.7, the equation only needs to be solved once for each function of interest, making the computational cost independent of the number of design variables. This technique is also known as the adjoint method, and its computational cost is proportional to the number of objective functions. The design variables can include, e.g., the sensitivity and the design direction with respect to the locations of the mesh nodes that define the geometry of the problem.

Focusing solely on geometry variations, we will only consider the subset of variables $\boldsymbol{x}$ that define the node positions in the mesh. In Equation 2.8, we can denote the right-hand side of the equation as the vector $\boldsymbol{c}$.

$$\mathbf{c} = \frac{\partial f}{\partial \mathbf{x}} - \psi^T \frac{\partial \mathbf{R}}{\partial \mathbf{x}} \tag{2.9}$$

After computing, the coefficients $\boldsymbol{c}$ provide sensitivity data for a sensitivity map mentioned previously in this chapter.

As a summary, the process for design iteration based on the adjoint method is outlined in a step-by-step list[34]:

1. A flow field is solved for the Navier-Stokes (N-S) equations, and the objective function f is evaluated.
2. The adjoint equation 2.7 is solved and fully converged.
3. Shape sensitivity data is calculated based on the Eq. 2.8.
4. A specific, small change to the geometry is chosen and applied. The expected change to the objective function f is computed using the sensitivity $\boldsymbol{c}$.
5. The flow field is solved again for a new geometry, and the difference between the new and the baseline objective function is evaluated.

As the magnitude of shape sensitivity decreases with each shape iteration, the shape converges towards an optimal objective function. A flow chart illustrating this methodology is provided in Fig. 2.3.

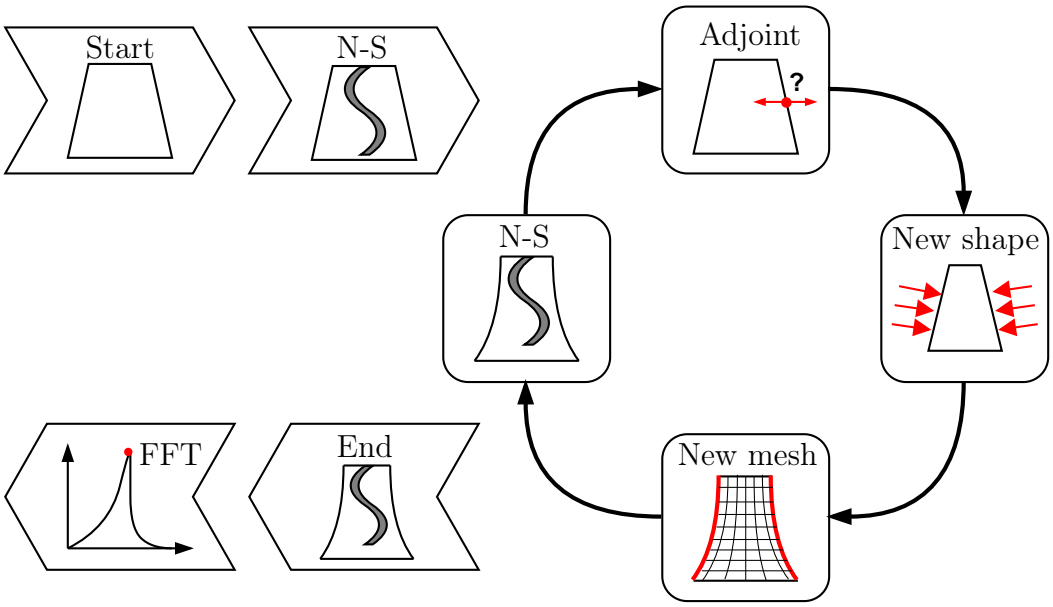

Figure 2.3: Flow chart for design iteration based on the adjoint method, based on Tzanakis[35]

2.2 Mesh morphing

In order to perform step 4 of the solution procedure outlined earlier, it is necessary to be able to modify the shape of the geometry and retain a valid computational mesh. Therefore, a mesh-morphing approach is adopted that is specific to ANSYS Fluent. All the details presented were sourced from the article by Han[34] and the ANSYS Fluent user guide[33].

In standard engineering problems, the shape sensitivity field may encounter smoothness issues that are not sufficient to define a shape modification.

Therefore, mesh morphing is employed in two ways. Firstly, as a smoother for the potentially noisy surface sensitivity field. Secondly, to ensure smooth movement of both the boundary and interior mesh. This approach is very attractive as it is applicable to arbitrary mesh cell types.

Typically, an optimization problem involves minimizing or maximizing the objective function while considering spatial constraints. Methods are required to produce a deformation field that is well-behaved and meets the manufacturability requirements while still allowing for locally sharper deformations where necessary to satisfy the imposed constraints. ANSYS Fluent offers three different morphing techniques for the adjoint solver: one based on polynomials, one utilising direct interpolation, and another using the radial basis function. Note that these methods are based on different design spaces and will therefore produce different morphing results.

A specific region is defined such that it encompasses all or a part of the problem domain. Only the mesh nodes within this area can move as a result of the morphing operation. Each method uses a different model to adjust the original mesh based on the sensitivities.

The polynomials-based approach distributes a regular array of control points over a control volume. Control points have a lower resolution relative to the mesh. Control points move in the direction of the sensitivity vectors. Bernstein polynomials and B-splines are used to map the control point motions to the nodes of the computational mesh. The control point motion for the Bernstein polynomials controls the large-scale smooth deformation, while the control point motion for the B-splines controls the fine-scale motions. These polynomials are later smoothed, and constraints are applied. Finally, the mesh is deformed to match to the field created by the polynomials. The exact equations used in this morphing approach can be found in the ANSYS Fluent user guide[33]. This method proves to be the most efficient while also producing the smoothest meshes; however, it is not suited for use with constraints. The process of mesh morphing using the polynomial-based approach is shown in Fig. 2.4 below.

The direct interpolation technique serves as an alternative to the polynomial-based approach. In this method, the deformation of the interior mesh can be viewed as a projection of the deformation from the boundary into the interior. The displacement of the interior mesh is calculated as a weighted average of all boundary node displacements, directing the mesh nodes directly according to smoothed sensitivities and fixed constraints. There are no curves that interpolate the calculated displacements. This approach is efficient under design conditions but results in a rough and imprecise mesh[33].

The last approach using the radial basis functions is a compromise between the two methods mentioned above. These functions determine the influence of the motion of a mesh node on its neighbours. The radial basis functions are functions ϕ whose value

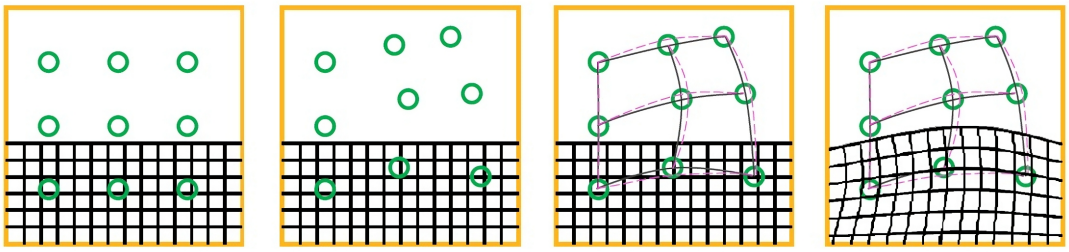

Figure 2.4: Polynomial-based approach to mesh morphing in ANSYS Fluent, control points are green and the mesh is black[33]

depends only on the distance between the input and some fixed point[36]. This group of functions includes, e.g.

- Gaussian function
$$\phi(r) = e^{-r^2}$$
- multiquadric function
$$\phi(r) = \sqrt{1 + r^2}$$
- inverse quadratic function
$$\phi(r) = \frac{1}{1 + r^2}$$

The kernel functions are responsible for ensuring smoothness during the deformation process and can be chosen in the settings. This approach produces relatively smooth meshes and can successfully handle complex design conditions.

This chapter has introduced the adjoint-based optimization method as a powerful tool for efficiently exploring complex design spaces. The method allows the automatic optimization of design variables by calculating sensitivities. Two approaches to formulating the adjoint equations have been discussed — continuous and discrete, with emphasis on the numerical consistency advantages of the latter.

The adjoint method involves solving the adjoint equations to obtain sensitivity information to guide shape optimization. Mesh morphing techniques, including polynomial-based, direct interpolation, and radial basis functions, play a crucial role in modifying the geometry while maintaining a valid computational mesh. Overall, the adjoint method, coupled with appropriate mesh morphing strategies, provides an efficient way to achieve optimal designs in engineering applications. This information will help to understand the exact process of using the adjoint method in ANSYS Fluent in the next chapter.

Chapter 3

Test case for the adjoint solver

Before carrying out a complete three-dimensional shape optimization of the draft tube, a simpler two-dimensional case was tested in order to evaluate the capabilities and limitations of the adjoint solver in ANSYS Fluent. The objective is to establish a detailed methodology for the adjoint optimization process. A different transient phenomenon had to be selected as the vortex rope cannot be fully captured in two dimensions. The well-known phenomenon of the Kármán vortex street was chosen since its periodic shedding can be captured reasonably well in two dimensions. The issue is that the adjoint solver is only capable of computing sensitivities for steady-state simulations. In order to resolve this issue, it was necessary to time-average the flow solution data to obtain a single flow state from which sensitivities can be calculated. The exact process of setting up the adjoint solver will be outlined later.

The objective of the test case was to optimize the shape of the bluff body with the aim of minimizing the drag coefficient c_d. The geometry includes a rectangular flow domain with a circular bluff body near the inlet. The types of boundary conditions, along with the dimensions of the geometry, are illustrated in Fig. 3.1.

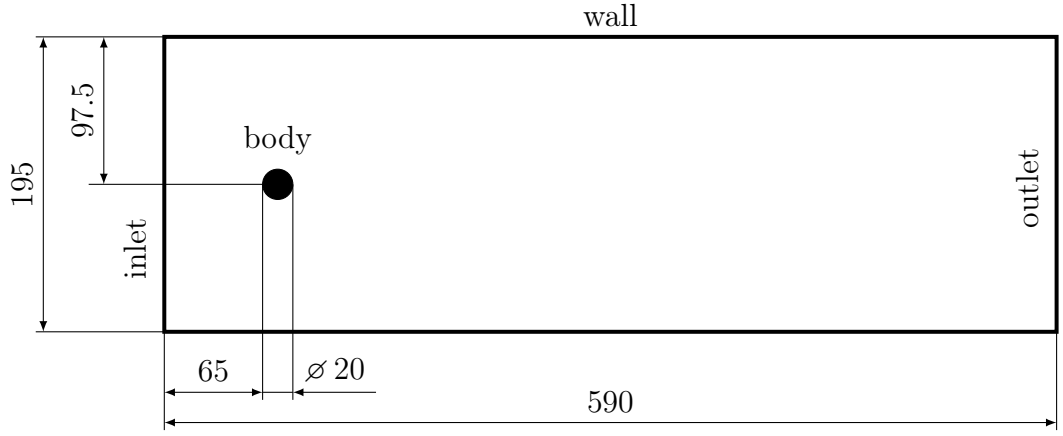

Figure 3.1: Dimensions of the flow domain (in millimetres) and the types of boundary conditions for the test case

The flow domain and the mesh were generated using SpaceClaim and ANSYS Meshing version 2023 R2. In order to create a structured quadrilateral mesh, a flow domain decomposition was necessary, with emphasis focused around the bluff body. The flow domain decomposition is illustrated in Fig. 3.2.

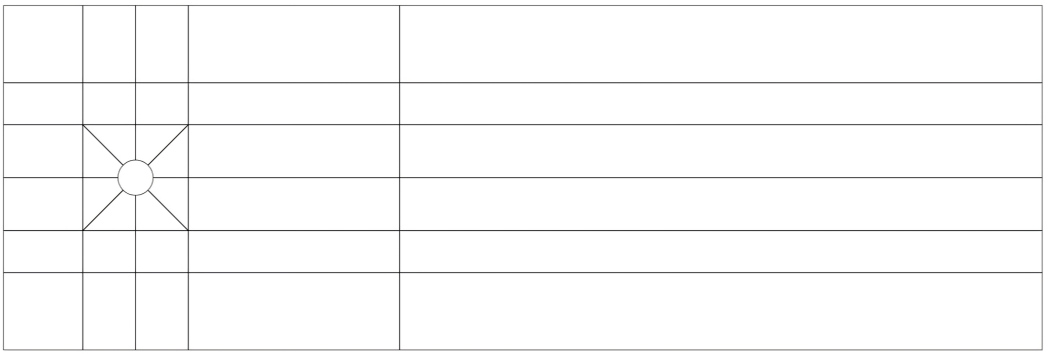

Figure 3.2: Decomposition of the flow domain

The boundary layer near the bluff body plays a crucial role as it is the source of the instability for the vortex shedding. Small vortices form on the surface of the bluff body during this instability, leading to the formation of rows of vortices in the wake. In order to capture this instability, the first layer element should be of minimal size. Additionally, in the wake region behind the bluff body, emphasis is placed on the element growth rate between adjacent elements. It is desirable to keep this parameter as low as possible to avoid unphysical vortex structures. Fig. 3.3 shows a detailed view of the mesh around the bluff body.

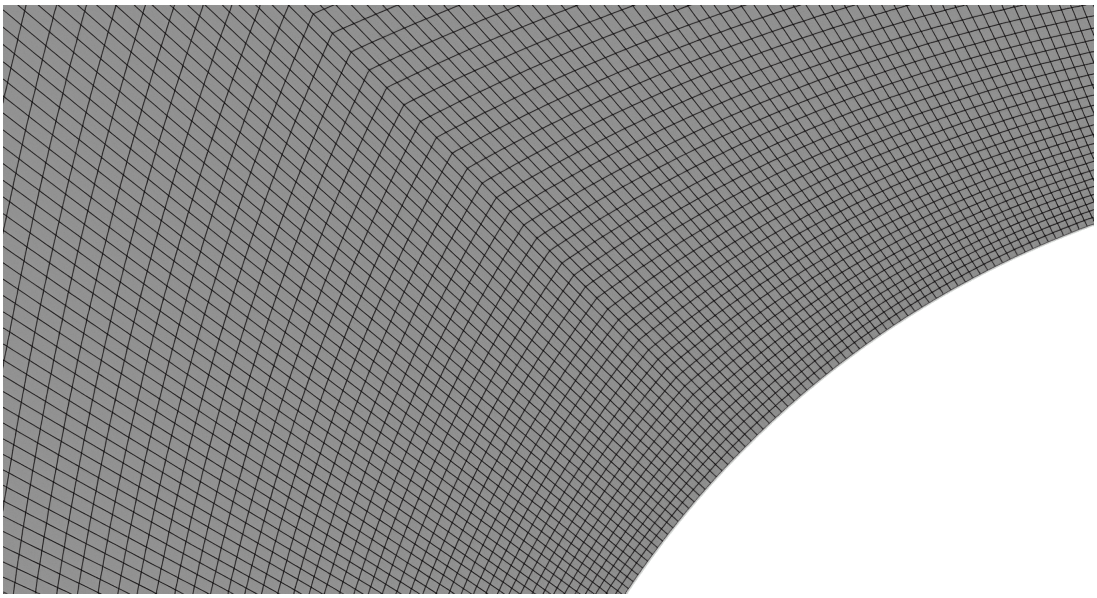

Figure 3.3: Detailed view of the mesh around the circular bluff body

The key mesh parameters are outlined in Tab. 3.1. All values except the maximal aspect ratio meet the theoretical recommendations. The recommended values align with widely accepted academic standards. The theoretically recommended maximum aspect ratio value is challenging to achieve in practice, with researchers commonly achieving values ranging from 20 to 50. The "recommended" number of elements corresponds to the maximum number of elements available in the student version of ANSYS.

The simulations were conducted using the commercial software Fluent, version 2022 R2. The medium in the fluid domain contains air with the default properties: density

Table 3.1: Summary of the mesh properties for the test case

Mesh Property	**Value**	**Recommended**
Element Count	249 400	$< 512\,000$
Maximal Aspect Ratio	7.6842	< 5
Maximal y^+	0.44	< 1
Maximal Skewness	0.5	< 0.9

$\rho = 1.225\,\mathrm{kg/m^3}$ and dynamic viscosity $\mu = 1.78 \cdot 10^{-5}$ Pa · s. The boundary conditions are outlined in Tab. 3.2. The flow velocity was experimentally determined to ensure ideal conditions for vortex shedding. The hydraulic diameter matches the height of the flow region.

Table 3.2: Boundary conditions for the test case

Inlet	**Wall**	**Outlet**
$v = 0.37$ m/s		$p = 0$ Pa
$D_h = 0.195$ m	No slip	$D_h = 0.195$ m
$I = 5\,\%$		$I = 10\,\%$

Firstly, a steady-state flow solution was computed as the initialization for the transient simulation. Subsequently, the transient flow solution was obtained by implementing the solver settings listed in Tab. 3.3. The k-ω SST turbulence model was selected for its reliability in low-Re as well as mainly boundary layer flows, which is critical for vortex shedding phenomena. Unfortunately, the QUICK momentum scheme is not compatible with the adjoint solver. Therefore, an alternative scheme was selected with consideration for efficiency and accuracy. The time step was calculated using data from a previous experiment and estimated as 1/200 of the vortex shedding period. The estimated value was further optimized through iterative process. Finally, the default number of iterations per time step was maintained.

Table 3.3: Solver settings for the test case

Turbulence modelling	k - ω SST
Pressure-Velocity Coupling	SIMPLE
Gradient	Least Squares Cell Based
Pressure	Second Order
Momentum	Second Order Upwind
Turbulent Kinetic Energy	Second Order Upwind
Specific Dissipation Rate	Second Order Upwind
Transient Formulation	Second Order Implicit
Time Step Δt	$2.5 \cdot 10^{-3}$ s
Iterations/time step	20

3.1 Setup of adjoint solver

As stated earlier in this chapter, the adjoint solver requires input from a steady-state flow solution. A viable solution is to utilize the Data Sampling for Time Statistics feature in ANSYS Fluent. This allows for the averaging of transient flow data over a period of time to obtain a single flow state for use in the adjoint calculation. To acquire accurate data, the sampling must follow three rules:

(a) Limit data sampling exclusively to the vortex shedding time period, excluding the transitional period between the initial flow and the onset of periodic shedding.

(b) Ensure that the sampling begins and ends in the same phase of the periodic shedding.

(c) Collect enough periods to obtain symmetrical flow data.

Two parameters, namely the drag coefficient c_d and lift coefficient c_L, were monitored on the bluff body to determine the onset of vortex shedding in the periodic phase, defined as

$$c_d = \frac{2F_d}{\rho\, v^2\, S} \tag{3.1}$$

$$c_L = \frac{2F_L}{\rho\, v^2\, S} \tag{3.2}$$

where:

F_d – Drag force, the force component in the direction of the flow velocity
F_L – Lift force, the force component perpendicular to the flow velocity
ρ – Mass density of air: $1.225\ \mathrm{kg/m^3}$
v – Flow speed of the fluid: $0.37\ \mathrm{m/s}$
S – Projected frontal area of the bluff body: height $20\,\mathrm{mm} \times$ depth $195\,\mathrm{mm}$

These parameters were used during the transient simulation to determine the correct time to begin and end data sampling. The mentioned methodology for data sampling is shown in Fig. 3.4. On the left-hand side, Fig. 3.4a shows how the drag coefficient c_d of a bluff body varies with time during vortex shedding, with the yellow-coloured region representing rule a), which specifies the data sampling process, limiting it to the periodic part of the curve. Fig. 3.4b shows the periodic part of the curve in detail and illustrates rule b): the red points show that the recorded signal begins and ends in the same phase of the periodic shedding and that a sufficient number of periods have been recorded to ensure a symmetrical mean flow solution. Additionally, the monitoring of the drag coefficient was necessary given that it is related to the function of interest for the adjoint solver. The drag coefficient will be used as a parameter to compare each newly shaped bluff body.

The final mean solution, containing the mean values of all flow parameters, serves as input for the adjoint calculation. Fig. 3.5 shows a comparison between the mean flow solution at the bottom and the instantaneous flow state on top, with the variables

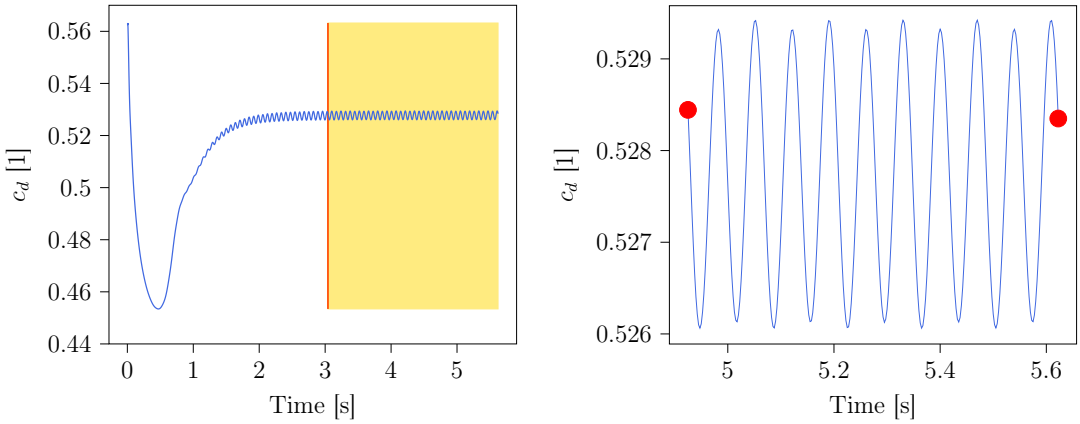

(a) Rule a: The yellow-coloured region highlights the periodic segment of the curve that is used for data sampling

(b) Rules b and c: The periodic segment of the curve has to start and end in the same phase of the signal, and a sufficient number of periods has to be recorded (zoomed for clarity)

Figure 3.4: Methodology for collecting the most accurate data for data sampling

velocity magnitude and mean velocity magnitude plotted. The figure shows that all vortices in the wake of the bluff body have been smoothed into a continuous flow field.

The current flow state remains the most recent instance of the transient simulation. As mentioned earlier, the adjoint solver is limited to steady-state simulations, meaning it computes shape sensitivities based on a singular flow state. Therefore, to use the adjoint solver, an additional step is required to impose the mean flow data as the present flow state and switch the transient setting to steady-state. The following procedure has been found to be reliable:

1. Create a Custom Field Function for each mean flow variable: mean x-velocity, mean y-velocity, mean pressure, mean turbulent kinetic energy k and mean turbulent eddy frequency ω.

2. Apply the recently created custom field functions to the flow field using the Patch function in the Initialization tab.

3. Switch from transient to steady state simulation.

The custom field functions act as a storage for the mean data that can later be directly applied to the flow field using initialization. At this stage, the adjoint solver can be set up for the shape sensitivity calculation. The first step involves defining an "observable," which is the function of interest defined in the previous chapter. ANSYS Fluent offers support for multiple observable types, including force, moment of force, swirl, pressure drop, surface, and volume integral of various quantities. Further information can be found in the Fluent user guide[33]. For this test case, the observable is defined as a force acting on the bluff body in the y-direction (drag force).

The adjoint equations are numerically solved using iterative methods, which is analogous to the solution process of the flow solver. The adjoint solver uses its own solver settings, and there are also residuals that need to converge. For accurate results,

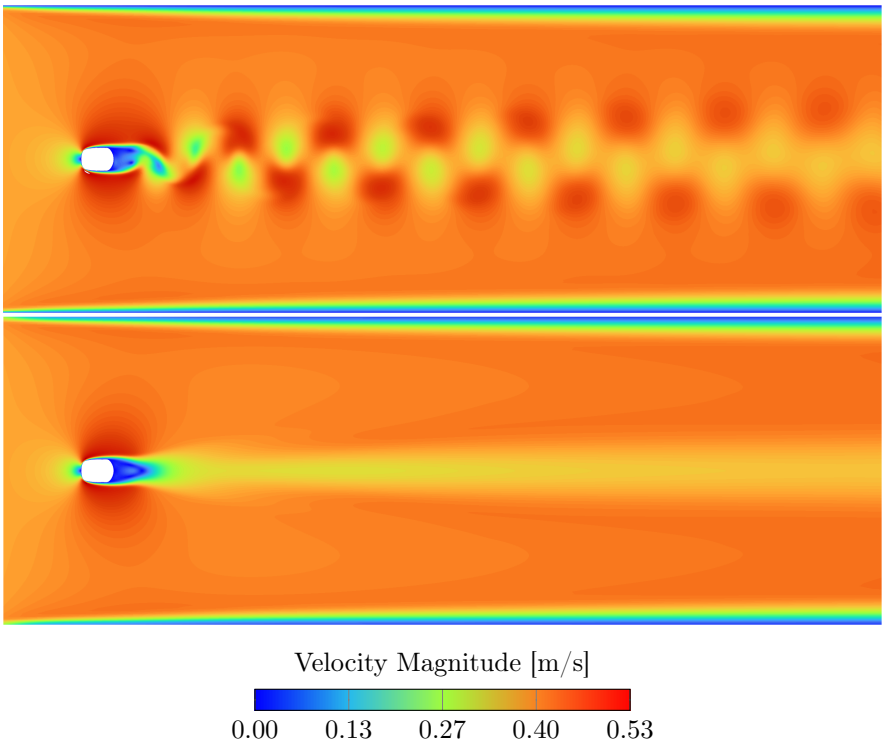

Figure 3.5: The instantaneous flow field during the transient simulation plotted using the velocity magnitude at the top, and the averaged flow field calculated during data sampling plotted using the mean velocity magnitude at the bottom

each adjoint variable's schemes must be the same or very similar to those used in the flow solver. This is why the QUICK scheme for momentum was not used for the flow solver, since it is not supported by the adjoint solver. Instead, the second order scheme was used for both flow and adjoint solver. The schemes for the gradient and pressure were copied from the flow solver settings. The remaining numerical settings, such as under-relaxation factors or the Courant number, were kept as the default settings. Tab. 3.4 provides a summary of the adjoint solver settings.

Table 3.4: Adjoint solver settings for the test case

Gradient	Least Squares Cell Based
Pressure	Second Order
Momentum	Second Order Upwind
Coupling	Partial

3.2 Shape optimization process and results

Once the solution process has converged, Fluent's built-in postprocessing tool can be used to analyse the calculated sensitivities. The adjoint solver calculates multiple sensitivities, such as sensitivity to mass sources, indicating where additional mass sources or sinks would have a positive effect on the observable, or sensitivity to energy

sources, indicating where heating or cooling would have an effect. The only sensitivity relevant in our case is the shape sensitivity, which indicates where the observable is sensitive to the deformation of the mesh. Units of sensitivity depend on the observable and the input quantity. In this case, the shape sensitivity to drag is being considered, meaning the units are N/m.

Fig. 3.6 shows the first results for the circular bluff body. On the left, the shape sensitivity is illustrated using vectors indicating both the direction and magnitude of the potential drag reduction at each point of the bluff body. The biggest shape sensitivity is located on the top and bottom of the bluff body. The shape sensitivity vectors can be traced back to the initial mean flow field. The plot on the right of the figure shows the mean static pressure around the bluff body. It can be seen that the low-pressure region (indicated in dark blue), where vortex shedding originates, corresponds to the greatest shape sensitivity.

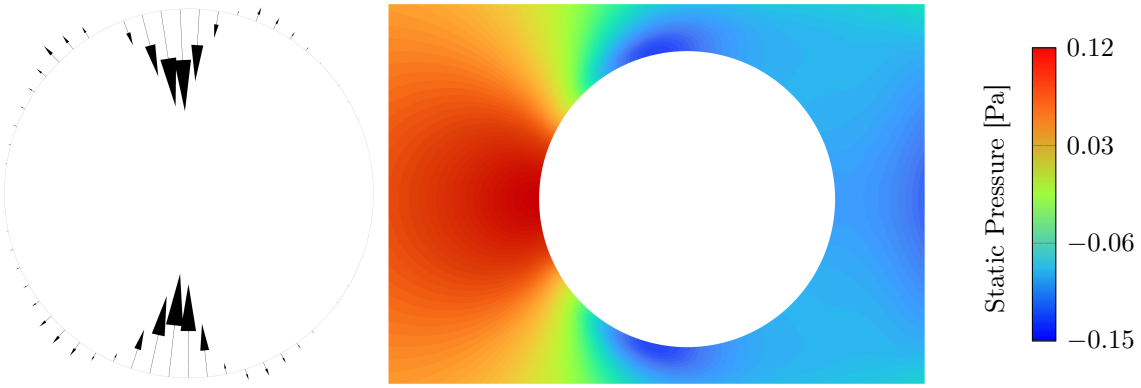

Figure 3.6: Shape sensitivity to drag calculated by the adjoint solver, on the left plotted using vectors, the mean pressure plot on the right as a reference to the calculated shape sensitivities

The final step in the shape optimization process is to calculate the mesh deformation based on the sensitivity data. This is done using the Design Tool, which is part of the Adjoint tab in Fluent. Multiple settings can be modified to control the mesh morphing process. All the steps required for the process are listed below:

1. Select one of the three available mesh morphing methods.
    - For the testcase, Radial Basis Function has been chosen as it gave the best results.
2. Define the mesh deformation domain that encompasses the bluff body.
    - The region should be sufficiently large to avoid constraining mesh deformation around the bluff body.
3. Define the optimization goal, a target change in value of the objective.
    - It is necessary to optimize the bluff body shape iteratively in small increments to avoid generating unphysical shapes. The first 4 shape iterations were created with a target drag reduction of 10 %, while subsequent iterations of only 5 %.

4. Define region conditions.
    - Force symmetrical mesh morphing, block deformation in a certain direction.
5. Set the numerics for mesh deformation.
    - Choose the kernel function, the inverse multiquadric kernel type was chosen; select the number of iterations and other parameters that are specific for each mesh morphing method.

Fig. 3.7 illustrates the configuration steps in Fluent step by step. Depending on the chosen morphing method, settings for step 4 and 5 may vary. In this 2D case, the radial basis function was selected due to its ability to produce good-quality mesh even after multiple morphing iterations, while also effectively handling large deformations. The region conditions and numerics were kept at their default settings.

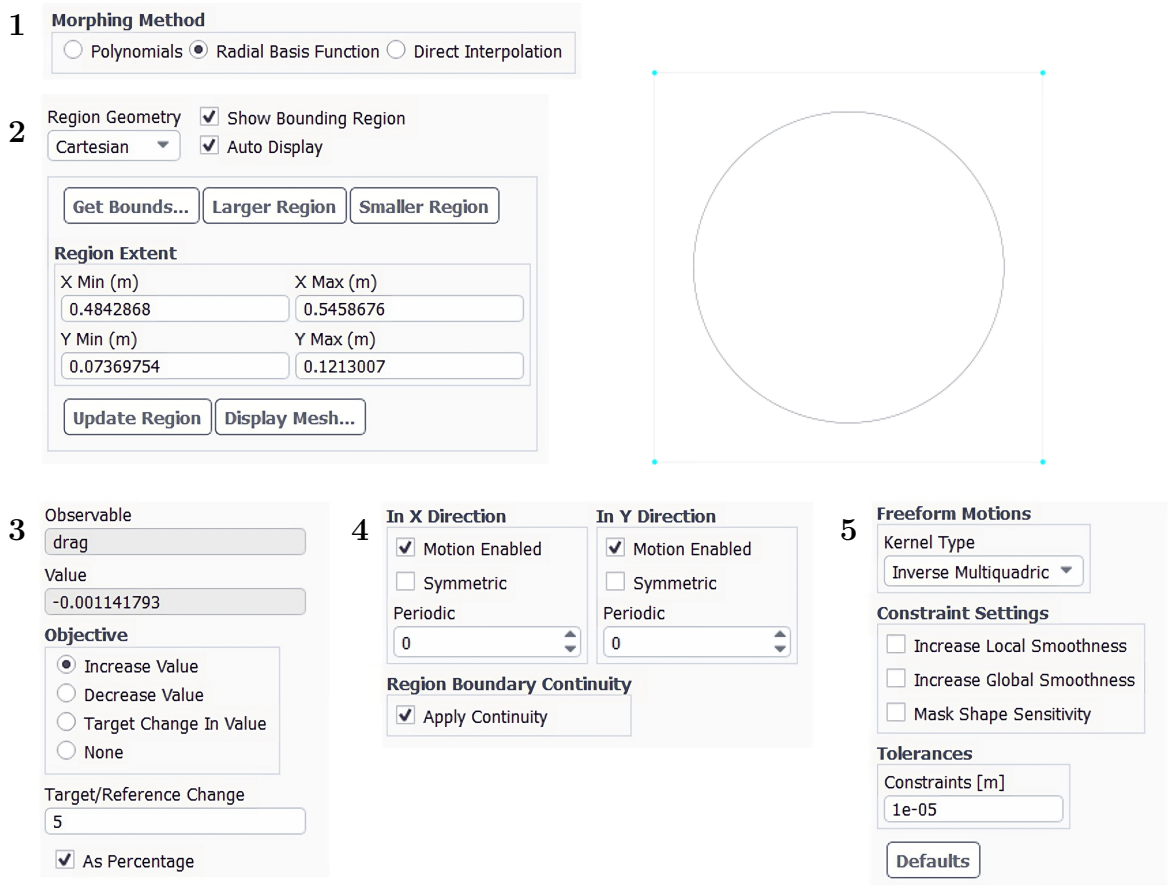

Figure 3.7: A step by step configuration process of the Design Tool in ANSYS Fluent with specific settings being shown; the bounding box around the bluff body is shown in step 2

At this point, all the required tasks have been completed and the design change can be calculated. Fig. 3.8 illustrates the comparison between the new bluff body shape and the initial circular cylinder. The deformation corresponds to the sensitivity vectors, as demonstrated in Figure 3.6. Although the change in shape is small, it can be attributed to the limited target drag change defined in step 3.

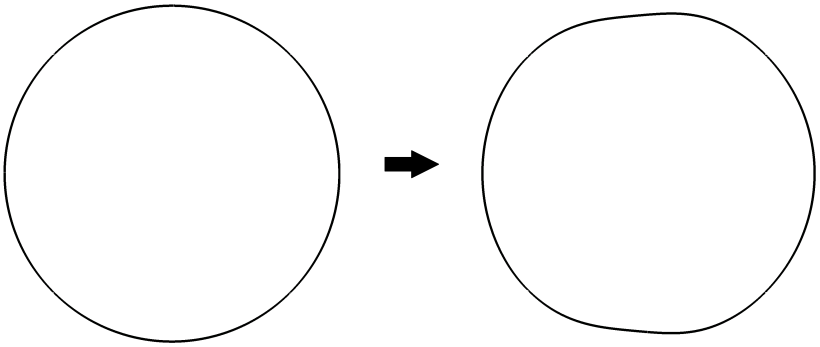

Figure 3.8: Original circular bluff body compared to the newly generated shape

Once the deformation has been checked, the mesh is adjusted through mesh morphing, a completely automatic process for the user. Figure 3.9 illustrates the mesh of the newly created bluff body. There is little visible difference to the naked eye, although changes can be observed after multiple mesh deformation iterations. The area closest to the bluff body experiences the most noticeable changes, while those further away remain unaffected.

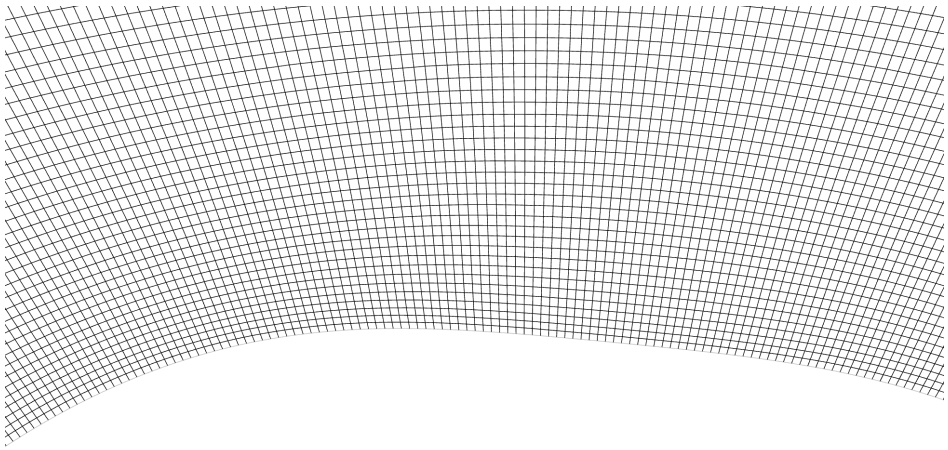

Figure 3.9: Mesh generated using mesh morphing for the new shape

To achieve the final optimized shape of the bluff body, this whole process has to be repeated multiple times. Once a shape has been generated, a new mean flow field, new sensitivity data, and a new mesh deformation must be calculated. The process continues until the drag coefficient of each additional shape converges to a limit. Design Tool tends to produce unphysical shapes at this point. Consequently, smaller optimization goals are necessary to avoid such behaviour. When drag reductions become sufficiently small, it indicates that the shape of the bluff body is approaching an optimized state.

Figure 3.10 illustrates the variations in the bluff body shape across the optimization process iterations, ranging from the initial circular shape through the intermediate iterations to the final optimized shape, which was reached after 11 iterations. A clear trend can be observed in the evolution, where the bluff body becomes thinner and takes on the form of a streamlined body, significantly reducing drag. It is worth noting that the thickness of the shape increases slightly at the trailing edge compared to the rest of the body. This could be attributed to the closer proximity of the vortex shedding origin

to the leading edge, as shown in Figure 3.6. In turn, sensitivities resulting from this phenomenon encouraged mesh deformation at this location rather than at the trailing edge. This effect was subsequently carried over to further iterations of the shape.

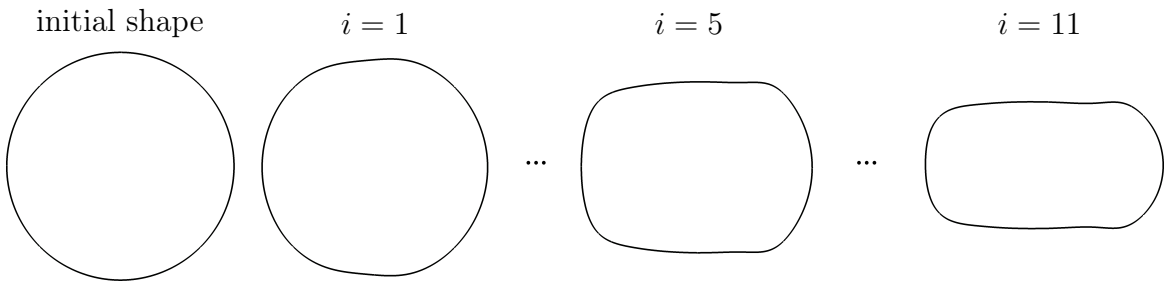

Figure 3.10: Evolution of the bluff body shape, from the initial circular bluff body to the last optimized shape, the number of iterations is denoted by i

Figure 3.11 demonstrates the changes in drag coefficient for each subsequent shape iteration. The plot displays the average drag coefficient $\bar{c_d}$ for each iteration. The average was calculated from the periodic portion of the signal generated during vortex shedding, as seen in Fig. 3.4a using the yellow box.

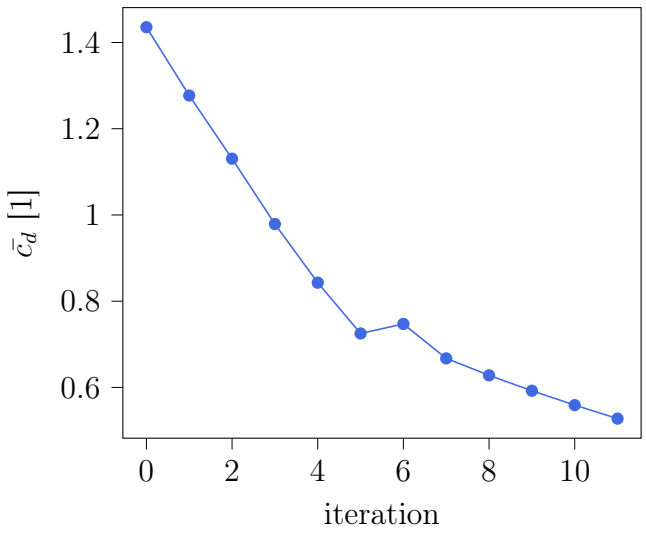

Figure 3.11: The change of the drag coefficient average $\bar{c_d}$ with each subsequent shape iteration, the drag reduction of each iteration corresponds partly to the target change defined in the Design Tool

A clear trend is noticeable, showing a decline in drag with each subsequent iteration. The only exception occurred during iteration $i = 6$ when the optimization goal of the Design Tool had to be readjusted from 10 % to 5 % due to the occurrence of nonsensical shapes. This sudden change in the target drag led to a sudden increase in drag. However, other bluff body shapes had a lower drag coefficient. The total reduction of the drag coefficient was 63 %, a decrease from 1.43 to 0.52. Further iterations could be calculated to reduce the drag even further, but by this point, each subsequent iteration would result only in a marginal reduction of the drag.

In this chapter, a comprehensive analysis of 2D shape optimization using the adjoint solver in ANSYS Fluent was conducted, focusing on the Kármán vortex street phenomenon as a test case. The initial phase of the study involved mesh generation and simulation setup, emphasizing the importance of capturing the boundary layer near the bluff body for accurate representation of vortex shedding. The adjoint solver, restricted to steady-state simulations, required a time-averaging approach to derive a singular flow state for sensitivity calculations. The setup of the adjoint solver involved defining an observable, ensuring compatibility with the flow solver, and establishing iterative convergence criteria.

The shape optimization process was systematically outlined, involving sensitivity analysis, mesh deformation, and iterative refinement. The results demonstrated a clear trend of drag reduction over consecutive iterations, culminating in a 63 % decrease in drag coefficient. The evolution of bluff body shapes showcased a progression towards a streamlined form, validating the effectiveness of the adjoint solver for this type of shape optimization. The detailed methodology and findings will serve as a framework for the following chapter that discusses the primary objective of this master's thesis: shape optimization of the draft tube.

Chapter 4

Adjoint shape optimalization of the draft tube

This chapter will deal with the primary objective of this master's thesis, the shape optimalization of the draft tube. The adjoint solver is used mainly in the automotive and aerospace industry, its use in the hydropower industry is rather limited. The goal is to test the potential of the adjoint solver for this type of optimization and analyze the resulting changes to the draft tube shape and flow field.

Rather than modelling the flow inside a Francis turbine, a simplified device known as a swirl generator will be employed for the simulations. While model turbines are necessary for researching the behaviour of a prototype, it is questionable whether investing in a model turbine is necessary for general research on the vortex rope. Nishi et al.[37] conducted measurements on a model turbine and found that even without the runner, characteristic features of the draft tube flow can be reproduced. These findings suggest that simple swirl generators can be used instead of model turbines when investigating the draft tube.

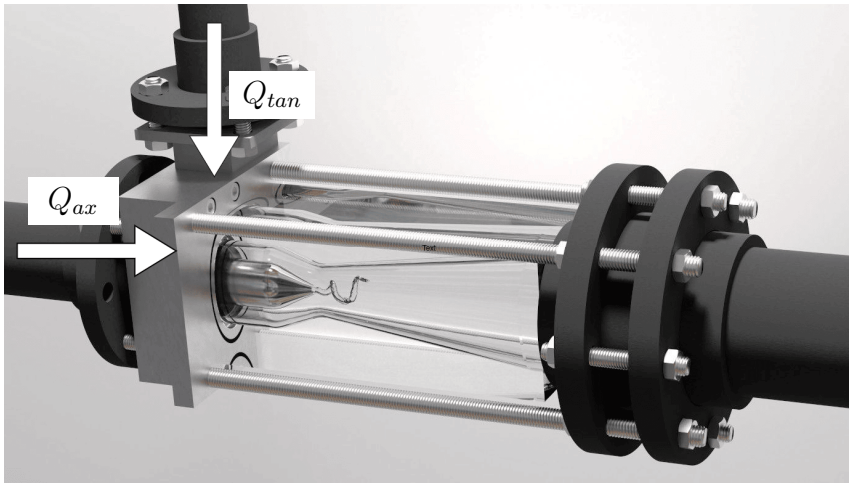

Figure 4.1: Swirl generator designed by Urban, swirling flow is generated by two inlet flow rates, Q_{ax} and Q_{tan}, image by Urban[3] (edited)

Swirl generators imitate the Francis turbine and are used in studies of the vortex rope. In the Francis turbine, the runner provides the swirling flow at the draft tube

inlet. However, for basic studies, various methods can be used to generate the swirling flow[38]. In this work, the swirl generator designed by Urban[3] was used, which generates swirling flow using two inlet flows: purely axial and tangential. The design of this swirl generator enables the control of swirl number by adjusting the ratio of the tangential flow rate Q_{tan} and the axial flow rate Q_{ax}. It consists of two inlets connected in a spiral case, a hub that acts as the turbine runner cone, and a draft tube that leads to the outlet pipe. At the tip of the hub, a vortex rope is expected to form. The complete design is shown in Fig. 4.1.

It is not entirely efficient to control the vortex rope's behaviour just by changing the shape of the draft tube. The hub acts as a source of the initial small vortices that form in the draft tube, which can lead to other instabilities such as vortex breakdown (discussed in Chapter 1) or Kelvin-Helmholtz instability, which develops at the shear layer between the backflow region and the main axial flow. The aim is to intervene in the area where initial instabilities form, which eventually lead to the formation of the vortex rope. This thesis will focus on the draft tube and the hub. Shape optimization will be carried out on these parts of the generator.

4.1 CFD simulations

The CFD simulations will model the unsteady Reynolds-averaged Navier-Stokes (URANS) equation in the swirl generator. For the purpose of this thesis, only a part of the complete geometry is used. This consists of the area surrounding the hub, the draft tube itself, and an additional outlet pipe to reduce the impact of the constant pressure boundary condition. This simplification can be made since the hub and the draft tube are the only areas of interest. This will also improve the computation time of the adjoint-based optimization due to its iterative nature.

The entire domain for the CFD simulations is shown in Fig. 4.2. The outlet pipe has been removed from the image for improved clarity. The pipe has a diameter of 106 mm and a length of 600 mm.

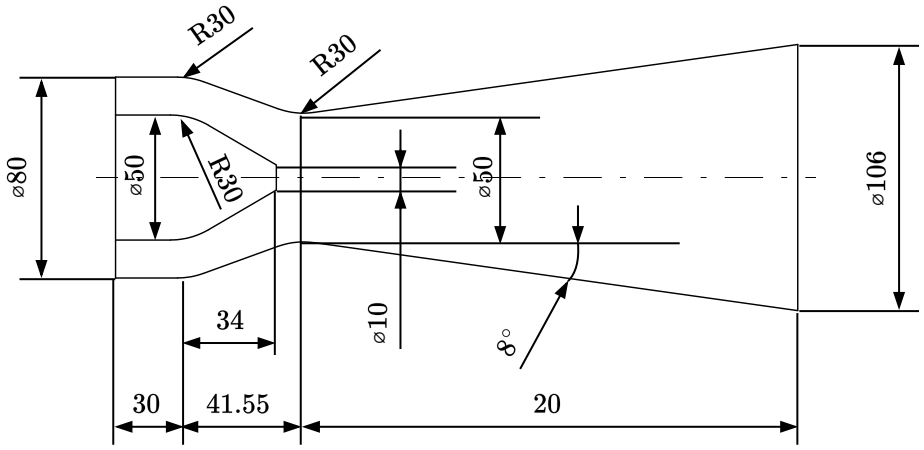

Figure 4.2: Domain for CFD simulations, outlet pipe removed for clarity

The computational mesh was created in ANSYS Meshing version 2023 R2. In order to capture the vortex rope behaviour accurately, a structured hexahedral mesh was

necessary. This was achieved by decomposing the domain using a standard pipe pattern, which consists of a square with slightly rounded edges in the center, and cutting the rest diagonally into four parts. This pattern allows for the generation of hexagonal cells with a low skewness. The decomposition is shown in Fig. 4.3.

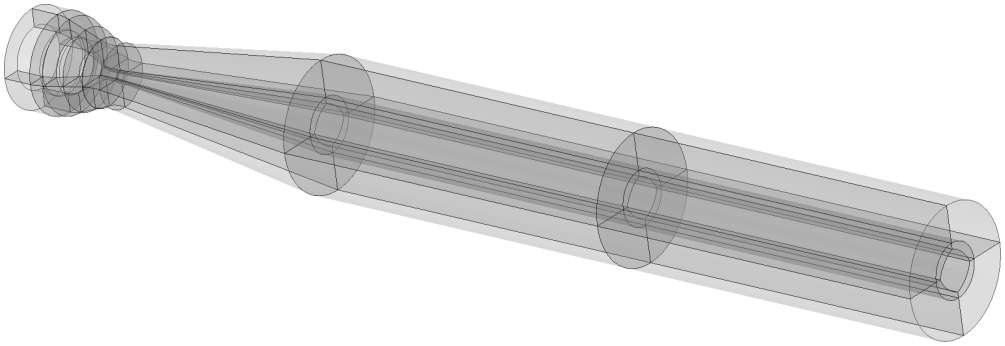

Figure 4.3: The decomposition of the whole domain

The mesh was generated by adjusting the "Number of Divisions" and "Bias" settings for Edge Sizing. This method provides control over cell density in different areas of the domain and enables the creation of a sufficient boundary layer around the walls. The main focus was on the region around the hub and the draft tube, where the vortex rope forms. The objective was to achieve low y^+ values and ensure smooth cell-to-cell transitions. On the left, Fig. 4.4 shows the hexagonal mesh of the annulus inlet with boundary layers from the top. The right image provides a detailed view of the mesh around the hub. The size of the rounded square in the middle of the hub was selected to maximize mesh quality. It can be seen that all the cells in that area have a good aspect ratio and smooth transitions between them.

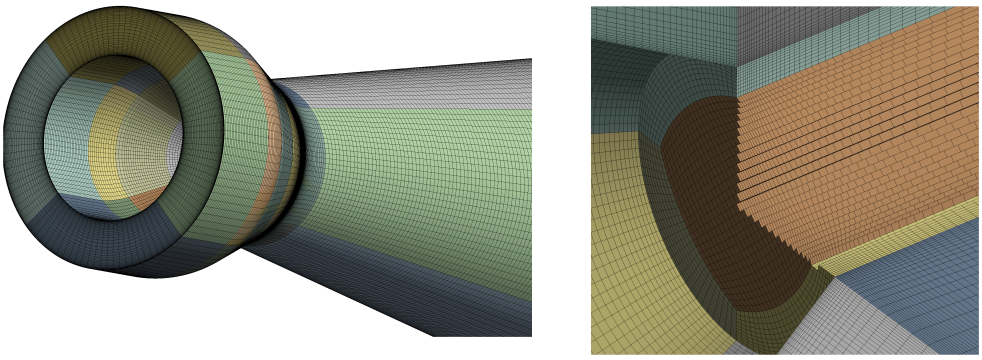

Figure 4.4: Computational mesh for CFD simulations, detail on the hub on the right side

The most important mesh statistics can be found in Tab. 4.1. The element count was limited by the hardware used for calculations. Although the maximal aspect ratio is higher, these cells are further away from the area of interest, so they will not have a significant impact on the results. The large difference between the hub diameter and the outlet pipe diameter is one of the reasons for the high value. The rounded square decomposition of the hub is connected with the same pattern on the outlet pipe. The uneven cell creation is caused by this discrepancy between diameters. The maximal

skewness is within acceptable limits, as mesh creation and decomposition were carried out with this parameter in mind.

Table 4.1: Summary of the mesh parameters

Mesh Property	Value
Element Count	2.4 million
Maximal Aspect Ratio	96
Maximal Skewness	0.52

Fig. 4.5 shows the values of y^+ on the walls of the draft tube and the hub. The lowest value of y^+ is 2, and the highest is 72. The cells with the highest values are only present in areas that have a low influence on the vortex rope behaviour. The image on the right shows that the values of y^+ on the hub are less than 10. Achieving this was one of the main goals since the hub is a critical area for accurate simulation, ensuring correct flow behaviour in the boundary layer of the hub.

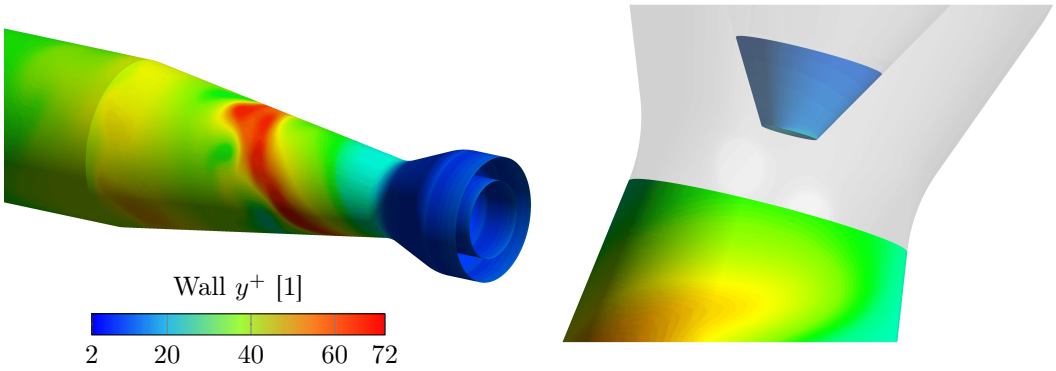

Figure 4.5: Detail of the y^+ contour on the walls of the draft tube (left) and the hub (right)

All CFD simulations of the draft tube were conducted using ANSYS Fluent version 2023 R2. The medium used in the fluid domain is water with the default properties: density $\rho = 998.2$ kg/m^3 and dynamic viscosity $\mu = 1.003 \cdot 10^{-3}$ Pa $\cdot$ s. Boundary conditions employed in this simulation are illustrated in Fig. 4.6 and summarized in Table 4.2.

Table 4.2: Boundary conditions for the draft tube

Inlet	Wall	Outlet
Velocity profile k and epsilon profile	No slip	$D_h = 106.6$ mm $p = 0$ Pa $I = 10$ %

The walls are subject to the no-slip condition, while the outlet is subject to the constant pressure boundary condition. The inlet boundary condition is defined by a

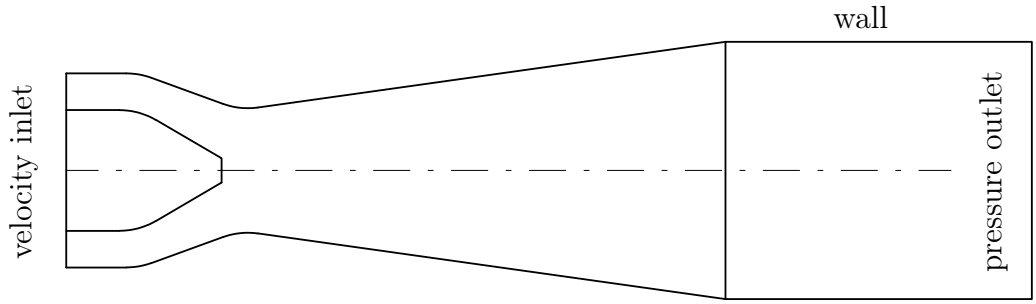

Figure 4.6: Summary of boundary conditions for the draft tube, velocity inlet uses a profile that defines radial, axial, and tangential velocity along the radius of the annulus inlet (not to scale)

profile of circumferentially averaged axial, radial, and tangential velocities, as well as turbulent kinetic energy k and turbulent eddy dissipation ε. The profile defines these variables as a function of the inlet radius. Circumferential averaging can help stabilize the vortex rope in the draft tube and increase the likelihood of achieving the desired axisymmetric shape of the draft tube. The profile used in this thesis was obtained from a steady k-ε simulation of the complete swirl generator, conducted by David Štefan. The generator parameters used in the simulation were the total flow rate $Q = 10$ l/s and flow rate ratio $Q_{tan}/Q_{ax} = 70 : 30$. Different inlet boundary conditions with varying flow rate ratios were tested to determine the optimal vortex rope conditions for adjoint optimization. The results showed that the 70:30 ratio yielded the best results in terms of the vortex rope size and shape. The inlet velocity, k and ε profiles are shown in Fig. 4.7. Some plot axes use dimensionless parameters, r/R is the dimensionless radius defined as

$$\frac{r}{R} = \frac{r}{r_{max}} \tag{4.1}$$

where r is the radius and r_{max} is the maximal radius of the current cross section, and $v/\bar{v}$ is the dimensionless velocity defined as

$$\frac{v}{\bar{v}} = \frac{v \cdot S}{Q} \tag{4.2}$$

where v is the relevant velocity, S is the cross sectional area of the current cross section, and Q is the volumetric flow rate.

Two turbulence models were tested to determine which one yields optimal vortex rope properties. The first model tested was the SST k-ω turbulence model due to its faster calculation times and widespread use in the industry. The results, however, showed that the model is too dissipative for swirling flow with a high degree of anisotropy, mainly due to the Boussinesq eddy viscosity assumption. As a result, the size of the resulting vortex rope was dampened by the model.

Therefore, the Reynolds stress model (RSM) was tested due to its ability to perform well for highly swirling, anisotropic flows, as it is not based on eddy viscosity. Another benefit of this model is its good convergence and satisfactory computational times. The results showed a larger vortex rope with a better resolved shape, and the periodic

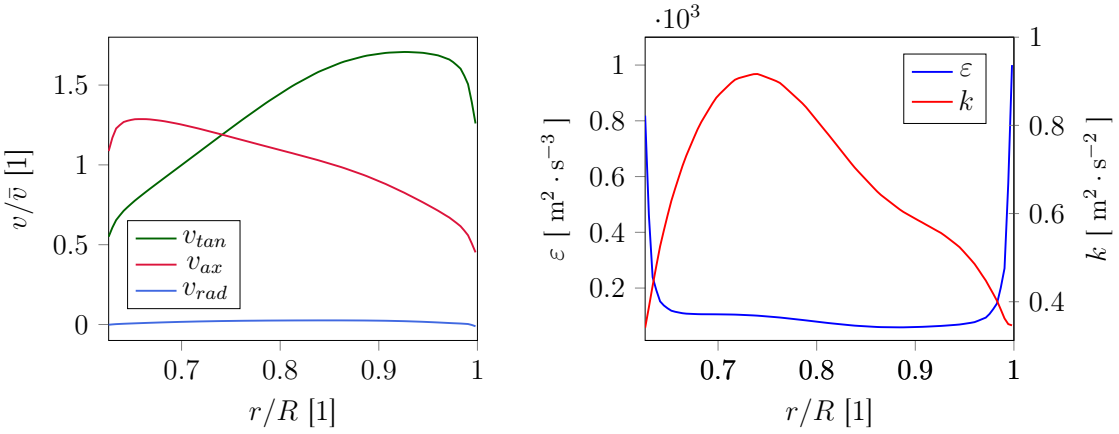

Figure 4.7: Inlet boundary condition defined by tangential velocity v_{tan}, axial velocity v_{ax}, radial velocity v_{rad}, turbulent eddy dissipation ε and turbulent kinetic energy k across the annulus inlet as a function of radius

rotation was more stable than SST k-ω. These results are consistent with previous research on CFD simulations of the vortex rope discussed in Chapter 1.

Similar numerical settings to those used in the test case were employed for all simulations, as they were found to be stable and reliable. The settings are summarized in Table 4.3. The quadratic pressure strain for RSM was tested to improve model accuracy; unfortunately, this model setting always resulted in divergence. The time step was estimated as 1/100 of the dominant period of the vortex rope rotation. This period was calculated as the inverse of the first harmonic frequency of the vortex rope. The frequency value was obtained from a previous study on the swirl generator conducted by Urban[3].

Table 4.3: Solver settings for the draft tube simulations

Turbulence modelling	RSM, Linear Pressure-Strain, Non-Equilibrium Wall Functions
Pressure-Velocity Coupling	SIMPLE
Gradient	Least Squares Cell Based
Pressure	PRESTO!
Momentum	Second Order Upwind
Turbulent Kinetic Energy	Second Order Upwind
Turbulent Dissipation Rate	Second Order Upwind
Reynolds Stresses	Second Order Upwind
Transient Formulation	Second Order Implicit
Time Step Δt	$1 \cdot 10^{-4}$ s
Iterations/time step	20

4.2 Adjoint calculation

The methodology used for the adjoint optimization of the draft tube is similar to that presented in Section 3.1. To avoid repetition, this section will focus on the differences.

The initial step was to use the Data Sampling feature in ANSYS Fluent, following the same three rules as in the previous test case. To determine the periodic time period of vortex rope rotation, the static pressure on the walls of the diffuser was measured at four different locations along its length. This allowed us to observe the vortex rope behaviour in real-time and determine when the motion became periodic, determining the start of the Data Sampling feature. On the left, Fig. 4.8 displays the static pressure contour in the diffuser during a transient simulation, clearly indicating the presence of a vortex rope. On the right, the mean pressure contour can be seen. The objective of obtaining axisymmetrical mean data has been successfully achieved by sampling data over multiple periods of the vortex rope movement. Obtaining axisymmetric mean data was crucial to ensuring an axisymmetric diffuser design, as the mean data have a direct impact on the adjoint sensitivity calculation and, consequently, the final shape change. Mean pressure, velocities, and turbulent variables were obtained for further calculations.

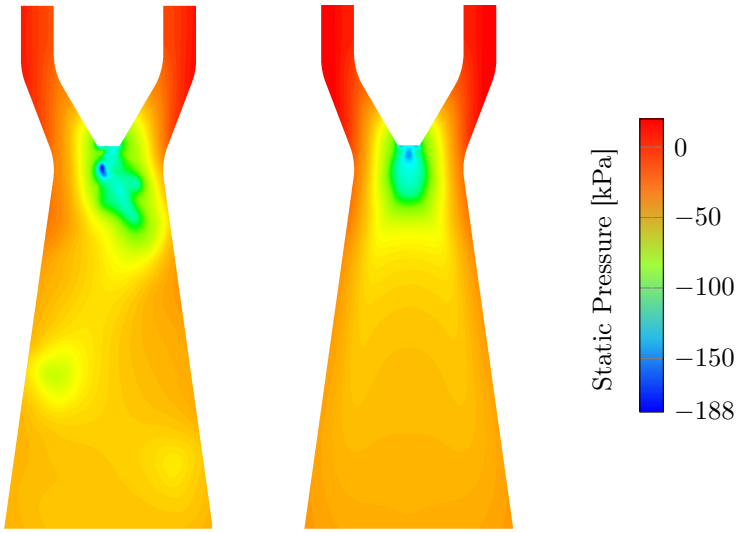

Figure 4.8: Data sampling for further adjoint calculation: left image shows a static pressure contour during a transient simulation, a vortex rope can be recognized; right image shows a mean pressure contour with an axisymmetrical shape

The objective function (observable) was selected from a limited list of functions supported by ANSYS in the adjoint solver. The available variables include force, moment, pressure drop, and swirl. In this case, swirl was selected as the most appropriate objective function. Swirl Sr for the adjoint solver is defined as the moment of the mass flow with velocity $\vec{v}$ relative to an axis defined by a point $\vec{r_c}$, and direction vector $\vec{d}$, it is expressed as

$$Sr = \iiint_V \rho \left(\vec{r} \times \vec{v}\right) \cdot \vec{d}\, dV \tag{4.3}$$

where V denotes the volume over which the integration is made, and $\vec{r}$ denotes the relative position to the point $\vec{r_c}$[33]. Fig. 4.9 specifies the control volume V and the axis used for the swirl calculation. The axis is defined by the point $\vec{r_c}$ and directional vector $\vec{d}$ on the axis of rotation z. Volume V is defined as the entire domain, excluding the outlet pipe. Vector $\vec{r}$ defines a point in V. Although the objective of the adjoint solver is to minimize swirl, it is important to note that swirl is not the only variable of interest. Other flow field parameters will also be analyzed.

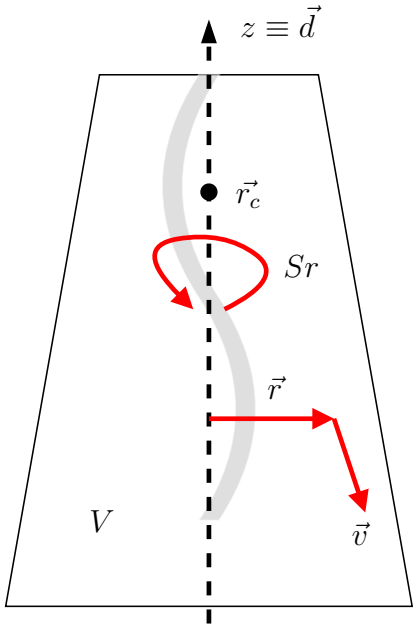

Figure 4.9: Variables defined for the objective function in the control volume V

The setup for the adjoint solver follows the same steps as outlined in Section 3.1. ANSYS recommendations for the adjoint solver were followed. When possible, the same numerical schemes as those used for the flow solver were used. The first-order scheme had to be used for momentum, as the second-order scheme led to divergence. All other settings were kept at their default values. The target residuals were below 10^{-3}, which usually indicates an acceptable adjoint solution. Tab. 4.4 summarizes all numerical schemes used in the adjoint solver.

Table 4.4: Adjoint solver settings for numerical methods

Gradient	Least Squares Cell Based
Pressure	PRESTO!
Momentum	First Order Upwind
Coupling	Partial

The Design Tool was used to calculate a new optimized shape of the draft tube based on sensitivity data from the adjoint solver. The tool required different settings than those used in the test case due to the increased complexity of the deformed geometry. The domain for the shape optimization was defined as the draft tube and the hub,

which are the main parts of interest as mentioned at the beginning of the chapter. The polynomial-based morphing method was chosen for its flexibility and numerical stability, particularly in cases with no constraints or other conditions. The other methods failed to reach the desired target value. Although the symmetry condition was tested, it only led to a significant increase in computational time. This was deemed not worthwhile since the axisymmetry of the final shape was already partially guaranteed by the axisymmetrical nature of the mean flow data. The target change of swirl for each iteration was set to a reduction of 10 % per iteration. A smaller change would result in minor changes to the geometry, requiring a large number of iterations. Larger changes would result in unsatisfactory shapes; the adjoint solver is intended for an iterative process with minor adjustments to the objective function.

In conclusion, this chapter outlines the primary objective of this master's thesis: the shape optimization of the draft tube using the adjoint solver method. CFD simulations were employed on a simplified swirl generator geometry to investigate the potential of the adjoint solver in optimizing draft tube shapes for improved flow behavior. The methodology for CFD simulations and adjoint calculations has been described, including mesh generation, boundary conditions, turbulence modeling, and adjoint solver settings.

The aim of these simulations is to explore the effectiveness of shape optimization in influencing the flow dynamics within the draft tube, ultimately resulting in improved performance and reduced instabilities. The following chapter will discuss the results obtained from the adjoint calculations, providing insight into the effectiveness of the optimization approach.

Chapter 5

Results

The process of adjoint shape optimization was carried out in six iterations, with no changes made to the settings for both the flow and adjoint solver between iterations. The number of iterations was limited due to consistent shape evolution. Fig. 5.1 shows the initial shape of both the diffuser (left) and the hub (right) in light grey and the final shape in dark grey. The magnitude of each shape iteration varied from 0.1 to 1 mm depending on the location. The initial conical diffuser shape transformed into a bell shape. This narrower diffuser shape stabilizes the vortex rope motion. In contrast, a wider diffuser shape makes the vortex rope unstable, resulting in the vortex rope adhering to the diffuser walls and, in turn, in irregular motion. The most significant modifications occurred in the upper half of the diffuser. This section has been transformed into a straight pipe, which then widens out to smoothly transition onto the outlet pipe. The changes to the hub's shape are more subtle. The walls of the hub have been brought closer together, resulting in a larger angle for vortex instabilities rolling off the hub. Overall, the hub has become slightly shorter.

Figure 5.1: Results of the adjoint shape optimization, both the diffuser (left) and the hub (right) are shown, the initial shape is in light grey and final shape in dark grey

The mesh was modified through the automatic mesh morphing within the Design

Tool. The mesh of the final draft tube shape is shown in Fig. 5.2. The mesh remained structured and hexahedral, with no change in the size of the boundary layer. However, the mesh became slightly twisted, the cells in the radial direction are not in a straight line. This small twisting may be caused by imperfections in the mean flow data, as they are not perfectly axisymmetric. Despite this, the mesh remained high-quality and is suitable for CFD simulations of highly swirling flow.

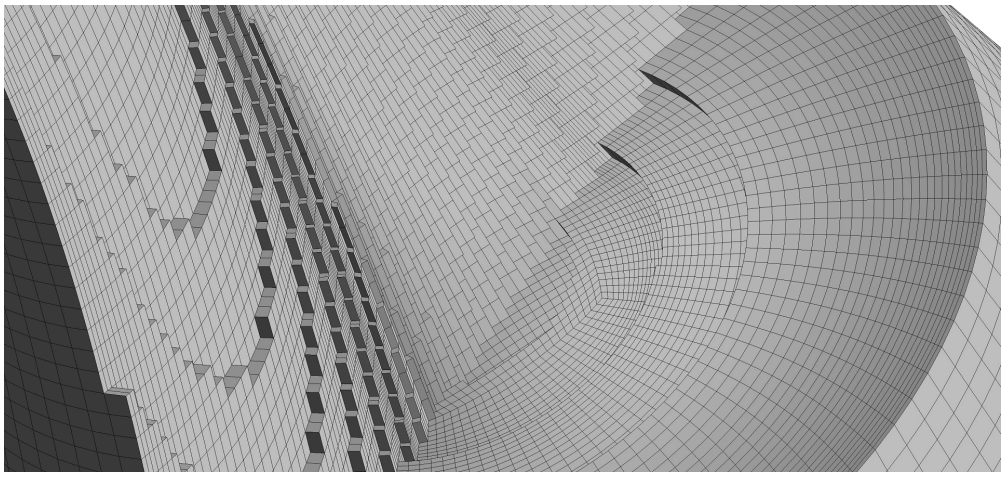

Figure 5.2: Computational mesh of the final draft tube shape

Fig. 5.3 shows the contour of y^+ for the final mesh. The value of y^+ has increased overall. On the hub, the average value has increased from 7 to approximately 11. This increase of y^+ should not significantly impact the results of the simulations and stems from its definition. The dimensionless wall distance y^+ is defined as

$$y^+ = \frac{y\, u_\tau}{\nu} \tag{5.1}$$

where u_τ is the friction velocity at the nearest wall, y is the distance to the nearest wall, and ν is the kinematic viscosity. The increase is caused by the smaller cross section of the draft tube in the final shape. According to the continuity equation, this results in a higher axial velocity for a constant flow rate, which in turn leads to a higher value of y^+, as seen from Eq. 5.1.

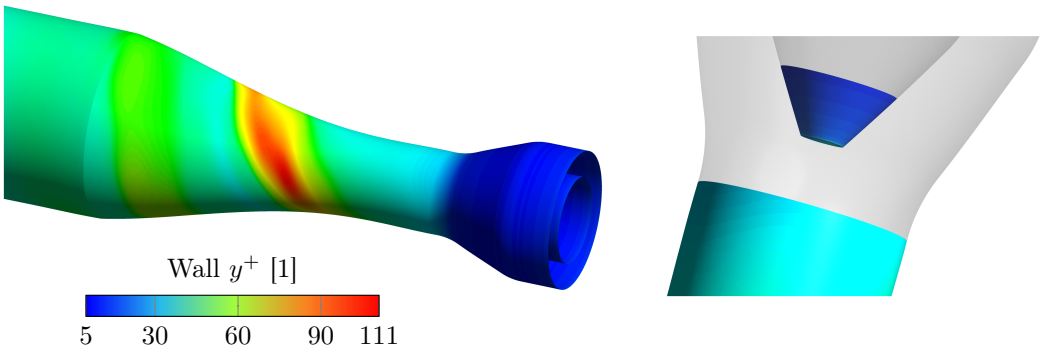

Figure 5.3: Contour of y^+ for the mesh of the final draft tube shape

The objective function for the adjoint solver Sr has decreased continuously with each iteration. Fig. 5.4 shows the changes in Sr throughout all iterations. On average,

it changed by around 2 to 3 %, with the exception of the step between iterations 4 and 5, where the decrease in Sr was by over 5 %. These values are lower compared to the intended decrease of 10 % defined at the beginning of the adjoint solver setup. This is understandable since the adjoint and flow solver are not mathematically tightly bound; differences may occur. The actual decrease calculated by the flow solver does not precisely match the intended decrease, which is expected due to the complexity of this non-linear optimization problem. After six iterations, the total decrease in Sr was approximately 18 %.

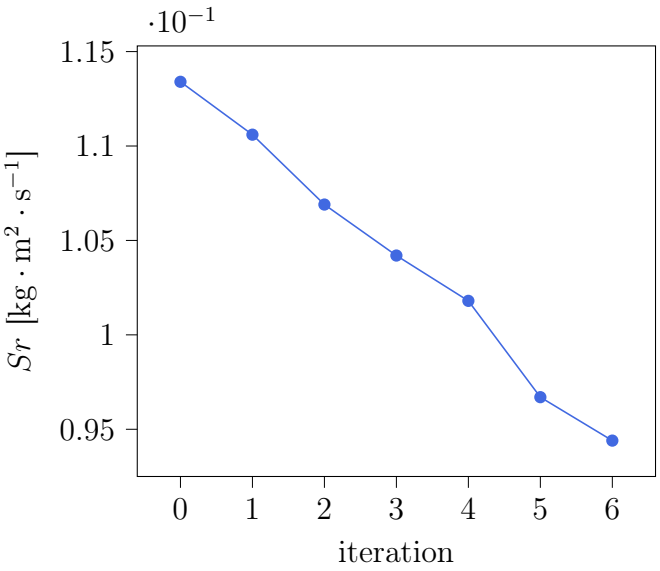

Figure 5.4: The adjoint solver objective function Sr change throughout shape iterations

Another result to be analyzed is the evolution of the shape and size of the vortex rope throughout each shape iteration. Fig. 5.5 presents a volume render of the vortex rope within the diffuser utilising instantaneous static pressure. It can be observed that the vortex rope underwent a process of elongation and straightening out with each iteration. This indicates that vortex lines have been straightened out as a consequence of the shape change. As the walls of the diffuser came closer together, the vortex rope was "pushed out" further into the diffuser. As the diffuser narrowed, the adverse pressure gradient was reduced, which, in turn, reduced the likelihood of creating the vortex breakdown instability. This should help stabilize the vortex rope motion.

Furthermore, the mean axial and tangential velocities along different cross-sections of the diffuser were analyzed. Mean values were the only viable option when comparing different diffuser shapes. Fig. 5.6 shows a series of plots of the mean axial velocity in the first column, the mean tangential velocity in the second column, and the current cross-section in the third column. The x-axis represents the dimensionless radius r/R, defined in Eq. 4.1, while the y-axis represents the dimensionless velocity $v/\bar{v}$, defined in Eq. 4.2. Negative velocity values indicate flow towards the outlet, while positive values indicate backflow within the diffuser. Each plot represents an evolution of the velocity profile in either the axial or tangential direction at the respective cross-section illustrated on the right side. The shape iterations are represented by a color bar on the bottom of the figure, with the lightest color representing the initial shape and the

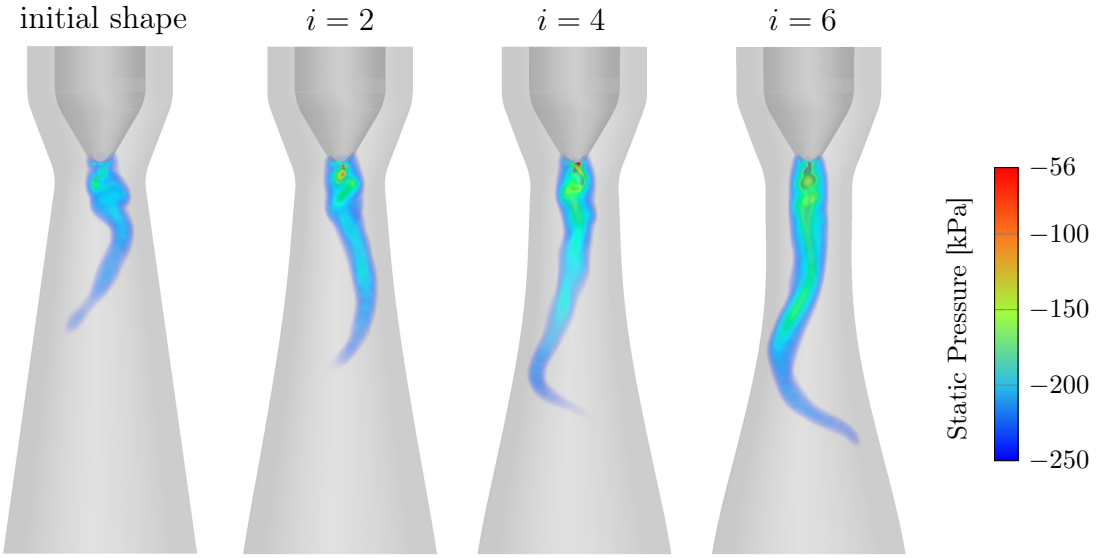

Figure 5.5: Volume render of instantaneous static pressure inside the diffuser, all shapes have the same scale, an evolution of the vortex rope shape can be seen

darkest color representing the final shape.

In the first two cross-sections, the axial velocity has increased significantly, with a marginal increase in the third cross-section. In the first cross-section, it can be observed that the velocity in the backflow region, situated in close proximity to the middle of the diffuser, has increased slightly, accompanied by a velocity increase around the backflow region. The most notable difference can be seen in the second cross-section, where the velocity profile evolved from an uneven shape with a small backflow region in the middle and large spikes on the walls of the diffuser to a more uniform profile along the radius. The velocity profiles of the last two cross-sections did not undergo significant changes throughout the shape iterations. The overall increase in axial velocity in the diffuser can be explained by the continuity equation, which states that for a constant flow rate, the velocity increases with a reduced cross-section area.

The tangential velocity has also increased, particularly around the center of the diffuser. This can be seen in the first two cross-sections. This phenomenon can be explained by the conservation of angular momentum, which states that for a reduced radius of the diffuser, the linear momentum must increase, resulting in a higher tangential velocity in the narrower cross-section. The velocity profiles remain relatively unchanged in the final two cross-sections.

The size and position of the backflow region in the diffuser and how it changed during the shape iterations were also examined. This region is of significant importance since it serves as the foundation of the vortex rope. Fig. 5.7 shows a volume render of the backflow (negative mean axial velocity). The region is moving downward with each iteration as the top region of the diffuser narrows. A similar trend could be observed in Fig. 5.5, where the evolution of vortex rope shape was studied. It can be observed that an energy transfer occurs as the core of the vortex rope moves away from the hub. The size of the backflow region remains relatively constant.

Another important parameter to be analyzed is pressure pulsations. Static pressure was measured on the walls of the diffuser at four different locations, as illustrated in Fig.

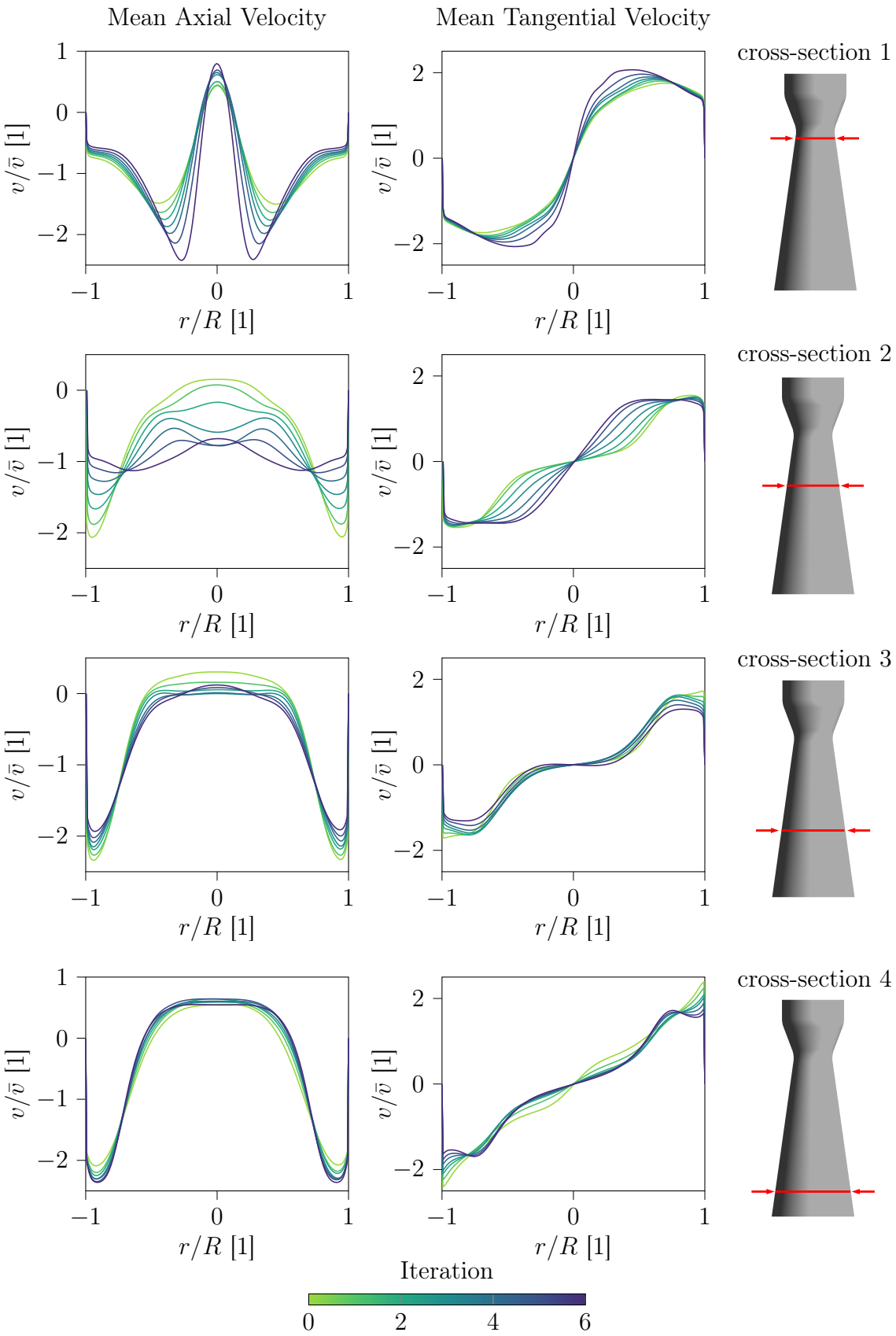

Figure 5.6: Evolution of mean axial and tangential velocity profiles at different cross sections along the diffuser, shape iterations are represented by color

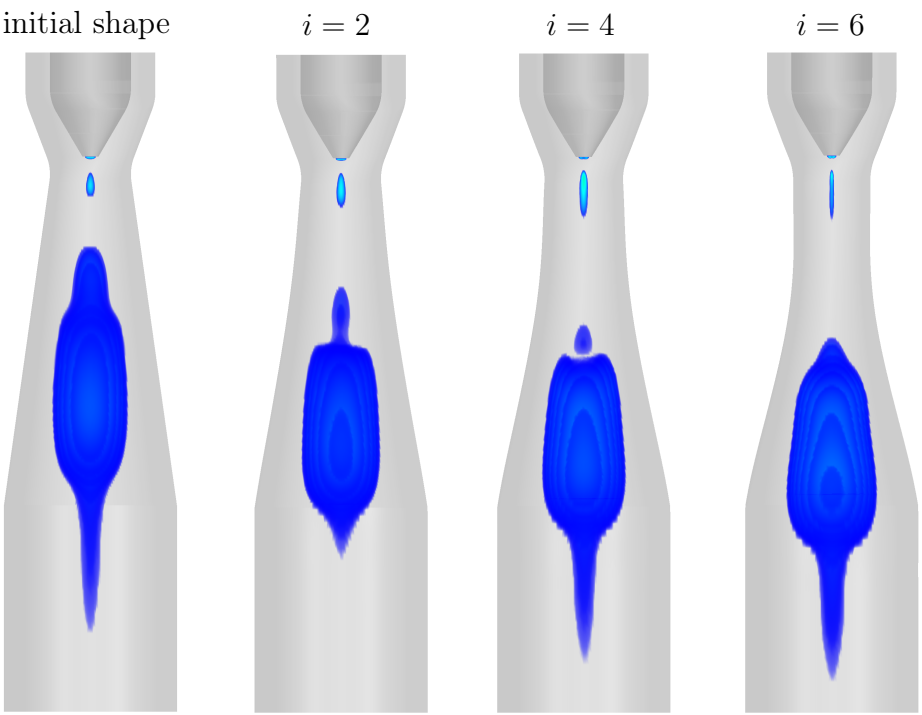

Figure 5.7: Volume render of the mean backflow region inside the diffuser during shape evolution, the region is moving downwards with each iteration

5.8 on the left. A representative sample of the measured signal is shown on the right side. The periodic nature of the vortex rope rotation can be recognized. All signals were processed using the discrete Fourier transform. Prior to this, the signals had to be modified to ensure accurate results in the frequency domain. It was necessary to allow an initial period of time at the start of the simulation for the vortex rope to fully develop. Once this period had elapsed, the signal became periodic, as shown in the plot. The initial portion of the signal was cropped to include only the periodic part of the signal. Coherent sampling was also taken into account during signal processing; it describes the sampling of a periodic signal where an integer number of its cycles fit into a predefined sampling window. Neglecting this can have a significant impact on the amplitude spectrum, with a potential reduction of up to 25 %. However, the values of harmonic frequencies are not affected by this. In order to ensure that the periodic signal has an integer number of periods, two conditions were enforced. First, after cropping the signal at the beginning, the end of the signal was also cropped so that the start and end points of the signal have equal values. Secondly, the start and end points must also have the same derivative signs. This ensures that the signal has the same value and phase at the start and end, and in turn has an integer number of periods. This kind of condition works for periodic, sinusoidal-looking functions. However, more complicated functions with many harmonic frequencies would require more advanced conditions to ensure coherent sampling, such as zero padding.

The results of the Fourier analysis are presented in Fig. 5.9. The frequency spectra are shown for the initial and final shapes of the first three monitors. The amplitude peaks and monitor locations for each plot are highlighted. The first harmonic frequency increased by 21 % from 46.7 to 56.7 Hz. This change can be attributed to the elongation

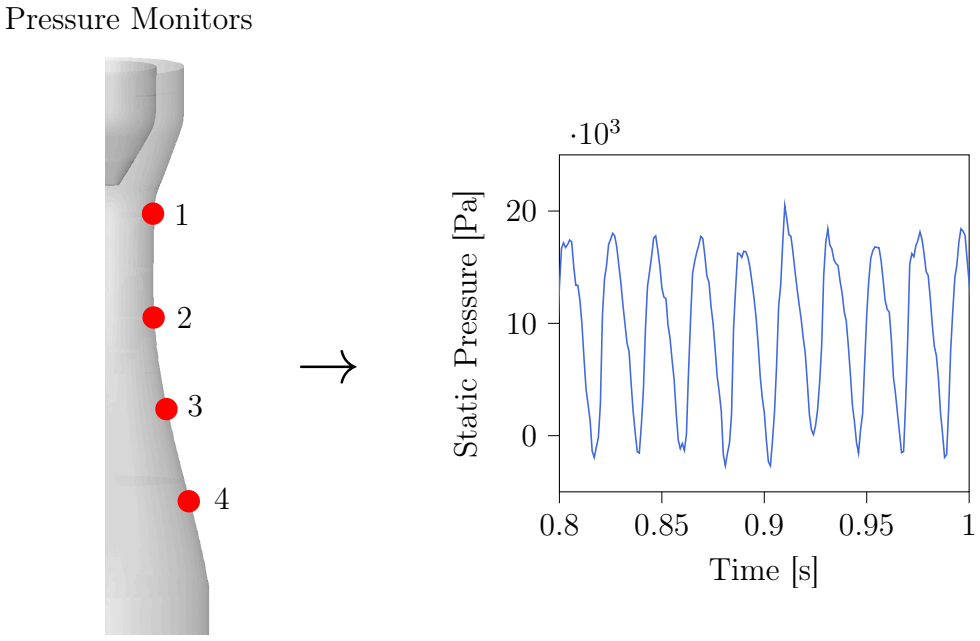

Figure 5.8: Four monitors of the instantaneous static pressure on the walls of the diffuser on the left, and a sample of the measured signal shown on the right

and straightening of the vortex rope with each shape iteration. The conservation of angular momentum states that with a smaller radius of the vortex rope, its frequency increases. A classic example of this phenomenon is how a figure skater in a spin draws in their arms and legs to increase their rotational speed. The harmonic frequency of the vortex rope in the initial shape was also compared to a simulation made by Urban[3] in his dissertation. During the development of the swirl generator, the vortex rope inside the draft tube was simulated using the full geometry of the swirl generator. The calculated harmonic frequency differed from that of Urban by more than 25 %. This indicates that different velocity boundary conditions at the diffuser inlet have a significant impact on the harmonic frequency of the vortex rope. The circumferentially averaged profile used in this work was an oversimplification to ensure accurate frequency results. Nevertheless, this discrepancy does not affect the qualitative outcome of the adjoint shape optimization. The initial point from which the adjoint optimization starts is not precisely defined, and an inaccurate harmonic frequency of the vortex rope should not yield significantly different draft tube shapes.

Another phenomenon that can be observed is the downward shift in the position of the maximal pressure amplitude. This effect can be more clearly observed in Fig. 5.10, which shows how the maximal pressure amplitude at the first harmonic frequency changed across the monitors during the shape evolution. The pressure peak of the initial shape was positioned at the first monitor, while the peak of the final shape was positioned at the second monitor. The plot demonstrates a gradual decrease in the pressure amplitude at the first monitor, accompanied by a steady increase at the remaining monitors. This indicates a downward shift of energy from the hub. This trend was previously observed in the analysis of other variables. However, the maximal amplitude for the final shape overall exceeded that for the initial shape. The adjoint optimization could not handle both aspects at the same time since the objective function is not directly correlated to the pressure pulsations. This phenomenon can be seen as a

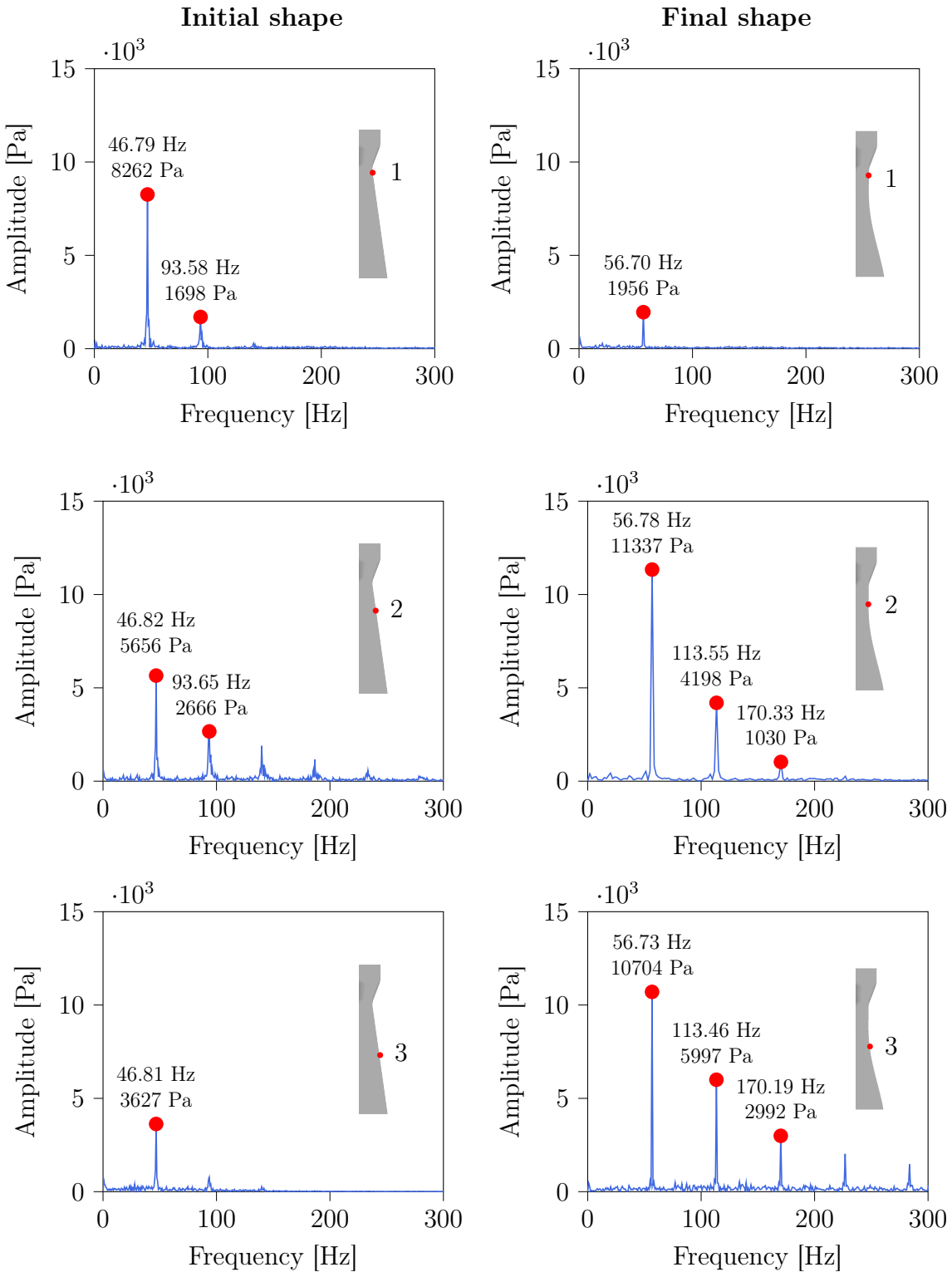

Figure 5.9: Frequency spectra from measured pressure signals, results from 3 monitors on the initial and final shape are shown

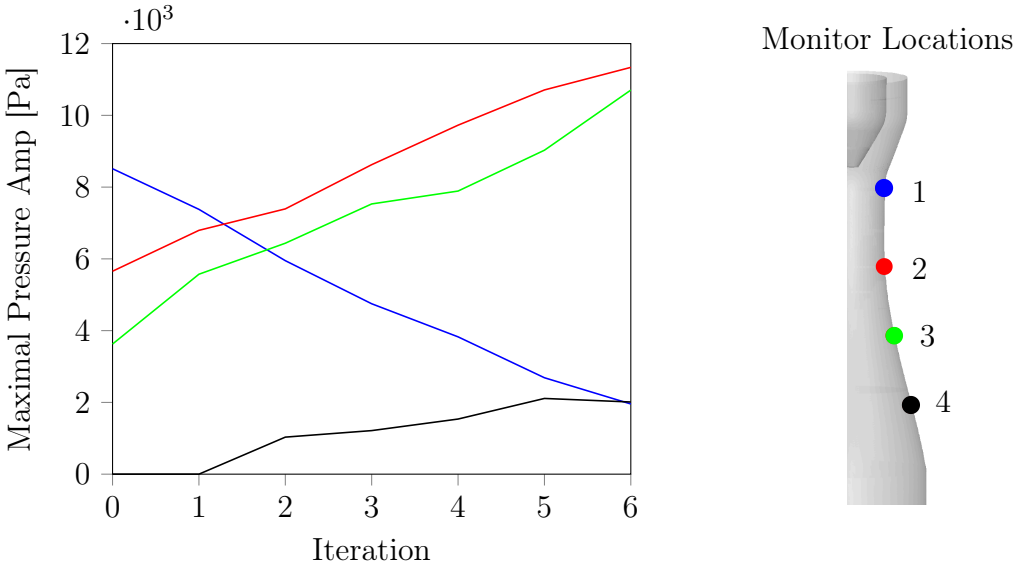

Figure 5.10: Maximal pressure amplitude of each monitor position during shape evolution, monitors and curves are linked by corresponding color

trade-off for the energy transfer away from the hub.

The swirl rate m across different cross-sections of the diffuser was monitored during shape evolution. The planes are located at the same height as the corresponding pressure monitors in Fig. 5.8. An equivalent definition to Eq. 1.2 was used for the calculation in ANSYS Fluent as follows:

$$m = \frac{\iint_S v_m \, v_u \, r \, dS}{R \iint_S v_m^2 \, dS} \tag{5.2}$$

where S is the cross-section for which the swirl rate is calculated. Fig. 4.9 illustrates how the time-averaged swirl rate changed at different plane locations throughout shape evolution. Overall, the swirl rate values have remained relatively stable, with only slight increases at plane 2 and small decreases at plane 1. These changes can be attributed to the aforementioned vortex rope elongation. A notable decrease can be seen at plane 4, which can be attributed to the fact that in the initial diffuser shape, the flow conditions created a backflow region that started close to plane 4. This contributed to the high swirl rate. As the shape evolved, the vortex rope elongated further, and the backflow region migrated downstream, resulting in a decrease in swirl rate. Swirl rate at other plane locations remained relatively constant. All values fell within a range of 0.7 to 0.8, which is considered a threshold in the literature when the flow is deemed unstable enough to facilitate the formation of a rotating vortex rope.

The vortex rope was also studied as a source of energy dissipation. Two variables were defined for this purpose. Firstly, the dissipation function will be defined as

$$\sigma = 2\mu \, v_{ij} \, v_{ij} + \rho \cdot \varepsilon \tag{5.3}$$

where μ is the dynamic viscosity, ε is the turbulent eddy dissipation, ρ is the density of fluid and v_{ij} is the strain rate tensor, defined as

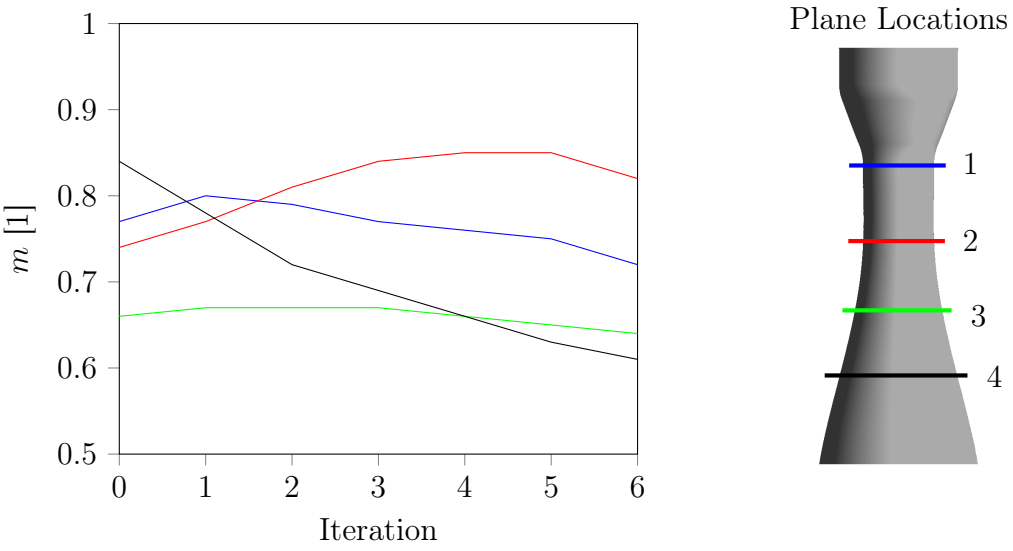

Figure 5.11: Time-averaged swirl rate m across four different plane locations

$$v_{ij} = \frac{1}{2}\left(\frac{\partial v_j}{\partial x_i} + \frac{\partial v_i}{\partial x_j}\right) \tag{5.4}$$

The dissipation function represents the energy loss per unit volume. The primary sources of energy loss are friction between the flowing liquid and the walls, as well as the vortices that are created during swirling flow, which irreversibly transform the kinetic energy into heat. In order to calculate the total power loss for a volume of fluid, the function is integrated over this volume as

$$\sigma_{vol} = \iiint_V \sigma \, dV \tag{5.5}$$

Secondly, the total power loss will be defined using total pressure loss at diffuser inlet and outlet as

$$\Delta P = \Delta p_{tot} \cdot Q \tag{5.6}$$

where Δp_{tot} is the total pressure difference at diffuser inlet and outlet and Q is the volumetric flow rate. The total pressure difference should represent the energy loss of the fluid between two cross-sections. Both variables represent the same phenomenon. The calculations were made for the mean flow variables.

It should be noted that there is a systematic difference in the manner in which the two definitions calculate the power loss. σ_{vol} employs a differential approach, calculating the power loss for a single point in a volume and then integrating the result over the volume to obtain the final result. ΔP, on the other hand, employs an integral approach, considering only the total energy of the fluid at the inlet and outlet of the volume. What happens between the cross-sections is not captured by the definition. However, in theory, when comparing the power loss calculated by these two definitions, the results should be identical.

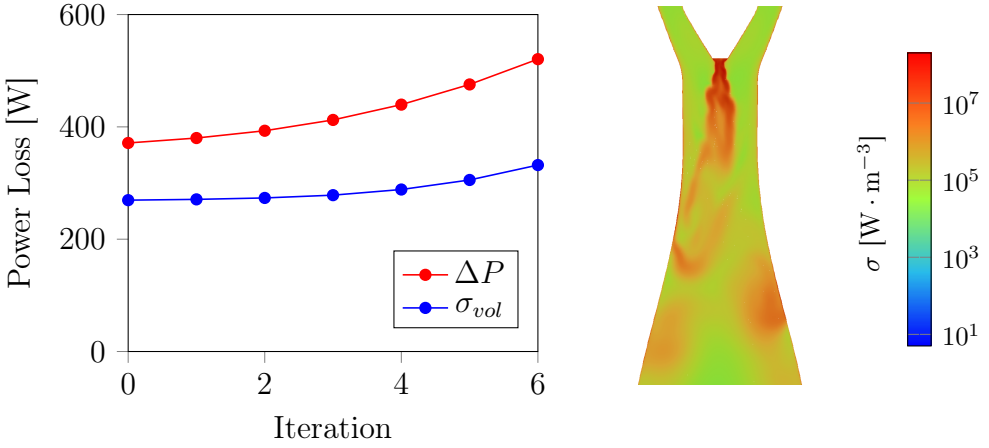

Figure 5.12: Mean dissipation function σ_{vol} and mean total power loss ΔP during shape evolution on the left, a contour of the instantaneous σ inside the diffuser on the right, the color scale is logarithmic

Fig. 5.12, on the left, illustrates the change in ΔP and σ_{vol} over shape iterations. Both variables have been time-averaged. It can be observed that the power loss increases with each iteration for both variables. This is due to the higher velocities inside the narrower diffuser, which increase the magnitude of the strain rate tensor v_{ij}. Furthermore, it is notable that there is a difference in the power loss between the variables. It is unlikely, that the discrepancy in the results is due to differing definitions of the variables; rather, it is likely to be due to the way in which RSM handles the near-wall modelling. As previously mentioned in Tab. 4.3, non-equilibrium wall functions were employed to model the near-wall flow. An accurate velocity profile near the wall is essential for accurate dissipation calculations. This has been a notoriously challenging problem for a long time. To address this issue, high-Re models such as the k-ε model or RSM employ the wall functions to artificially calculate the near-wall velocity profile, rather than modelling the flow itself. However, the non-equilibrium wall functions employed in these models are arbitrary functions that are not derived from fundamental physical principles. Consequently, discrepancies may arise, as illustrated in the plot. On the right, the plot shows a contour of instantaneous σ across the diffuser. It can be observed that, in addition to the walls, the vortex rope acts as a strong dissipation source, particularly near the hub.

The last variable to be analyzed is the pressure coefficient c_p, which can be used to evaluate the efficiency of the draft tube. It is defined as

$$c_p = \frac{p_2 - p_1}{\alpha_1 \, \rho \, \frac{v_1^2}{2}} \tag{5.7}$$

where index 1 represents the diffuser inlet and index 2 the diffuser outlet. Pressure values for both cross-sections are calculated as a mass-weighted average over the cross-section. The Coriolis number α is a dimensionless parameter that expresses the ratio of the actual kinetic energy to the ideal kinetic energy expressed by the mean cross-sectional velocity v_1. In this case it is used to refine the calculation. The Coriolis number is defined as

$$\alpha_1 = \frac{\iint_{S_1} |v|^2 \cdot v_z \, dS}{v_1^3 \cdot S_1} \tag{5.8}$$

where $|v|$ is the velocity magnitude, v_z is the z-velocity and S_1 is the cross-section of the diffuser inlet. Fig. 5.13 shows how the pressure coefficient c_p changed over the shape iterations. The c_p values shown for each shape were averaged over time during the periodic motion of the vortex rope. The pressure coefficient remained constant throughout the shape evolution, the values have remained in the range of 0.53 to 0.55. During optimal operation of a Francis turbine, the pressure coefficient values are around 0.9. Although energy losses in the form of heat have increased, as seen in the analysis of σ_{vol} and ΔP, the constant trend of the pressure coefficient c_p shows that the efficiency of the draft tube has not dramatically decreased. This is a positive effect for the operation of a Francis turbine.

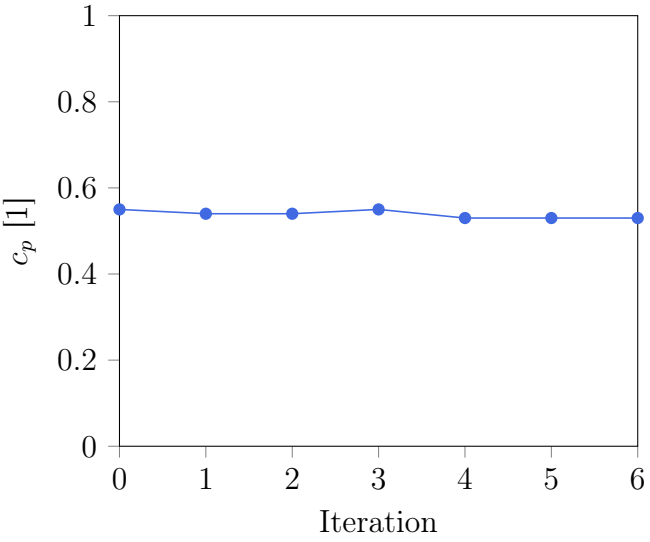

Figure 5.13: Time-averaged pressure coefficient c_p during the shape evolution, the values have been averaged over time for each shape

This chapter presented the results of the adjoint shape optimization, showcasing six iterations of draft tube shape evolution. The transformation of both the diffuser and hub shapes was described, highlighting how the diffuser's conical shape evolved into a stabilizing bell shape, while subtle adjustments were made to the hub. Mesh modifications, particularly mesh twisting, and changes in y^+ values were discussed in relation to the final draft tube shape. The reduction in the objective function Sr, indicating optimization success, and the evolution of the vortex rope shape were analyzed. Additionally, changes in velocity profiles, pressure pulsations, swirl rate, energy dissipation, and pressure coefficient were examined throughout shape iterations, providing insights into the draft tube's efficiency.

Chapter 6

Discussion

The methodology of the adjoint shape optimization was initially tested on a case presented in Chapter 3. The objective was to assess the reliability of the approach utilising mean variables for the calculation of the optimized shape. The effectivness of the method was of demonstrated, given that it was a straighforward two-dimensional case of external shape optimization. External shape optimization is a task for which the adjoint method was originally developed. In this case, the adjoint method yielded satisfactory results.

The draft tube shape optimization is a more complex task since the geometry is three-dimensional and the flow is highly unsteady. It was therefore unclear if the methodology would work in the intended way for this case. One question was whether the mesh morphing feature would be effective for a three-dimensional geometry. In particular, it was necessary to determine whether the quality of the mesh would be preserved in comparison to the two-dimensional test case. A mesh with a slight skew was generated, and the skewness of mesh cells increased with each iteration. This was mainly due to the slight asymmetry of the mean flow boundary condition of the adjoint solver. To dampen this effect, more periods could have been sampled to obtain more symmetric mean data. However, this approach is time inefficient and would have a minimal impact. The quality of the mesh was evaluated as satisfactory and no further changes to the mesh were performed. In any case, the skewness of the final mesh was so small that its effect on the results was essentially negligible.

Prior to the draft tube shape optimization, it was hypothesised that the adjoint solver would modify the shape into a narrower one. This modification would reduce the adverse pressure gradient (i.e. the backflow) that causes the vortex breakdown instability, which in turn is the source of the vortex rope. Narrowing the diffuser also straightens the vortex tube inside the diffuser. The resulting optimized shape of the draft tube confirmed this hypothesis. Two main features of the final shape have been observed.

1. The bell shape of the draft tube

    - The energy of the vortex rope was transferred away from the hub, resulting in a narrower and longer vortex rope. However, the negative effects of the vortex rope, such as pressure pulsations, were not mitigated.

2. Overall increase of the axial velocity in the diffuser

- The energy dissipation in the form of heat increased, yet this did not result in a change in the pressure coefficient c_p.

The shape of the hub was expected to have a large impact during the shape optimization process. The hypothesis was that intervening in locations where initial small vortices are generated would have an impact on how the vortices interact in the draft tube, which could change the character of the vortex rope. However, this hypothesis was not confirmed; on the contrary, the shape of the hub has undergone minimal change, indicating that it is not a crucial factor in the adjoint shape optimization process. It would be of interest to examine whether a different optimization algorithm with a different objective function would yield different hub shape results.

The results were influenced by several factors. One of the simplifications made during the simulations was the complete neglect of the influence of cavitation inside the vortex rope. As discussed in Chapter 1.3, research on this topic shows that multiphase CFD models better predict vortex rope characteristics and behaviour. This discrepancy was deemed acceptable since simulating multi-phase flow is computationally expensive and not feasible in combination with an iterative optimization process.

Another factor that influenced the results were the boundary conditions, specifically the velocity profiles at the inlet of the diffuser. In order to numerically stabilise the simulations and further improve the adjoint shape optimization, the profiles were circumferentially averaged. However, it was determined that this simplification was the main source of inaccuracies in the results. For example, when comparing the calculated frequency of the vortex rope with a simulation of the whole swirl generator by Urban[3], discrepancies in the frequency were found. The main difference between the simulations is the boundary condition at the draft tube inlet. Reducing the full two-dimensional velocity profile to a circumferentially averaged profile proved to be an oversimplification. It would, of course, be optimal to use a real velocity profile measured inside the draft tube of a Francis turbine; however, this data was not available.

It is important to note that alterations to the shape of the draft tube can have a significant impact on the overall performance of a Francis turbine. These changes can affect the turbine's maximum efficiency and the optimal operating point, which can be shifted to a different flow rate.

From the nature of the problem, it follows that the methodology of suppressing the vortex rope by changing the shape of the diffuser can never completely suppress the vortex rope. This is because the source of the vortex rope, namely the large tangential velocity components coming from the runner of the Francis turbine, cannot be eliminated solely through the modification of the diffuser shape. Consequently, the swirling energy coming from the runner can only be redirected in some manner. This must be taken into account when analysing the results.

The question thus arises as to whether the adjoint method is suitable for this type of shape optimization. The capabilities of the adjoint solver were tested as part of this master's thesis. In engineering, the adjoint method was originally developed for the optimization of external aerodynamics, specifically in the automotive and aviation industry. In the hydropower industry, the adjoint solver has not seen much use. There is no research regarding the use of the adjoint method in the shape optimization of the draft tube. One success of the presented results is the reduction of the objective function, swirl, by 18 %. This is an unusual objective function since usually the objective functions used in the automotive and aviation industry are drag, lift, or pressure drop.

This confirmed that the adjoint solver is capable of achieving the intended goal even when using non-standard objective functions. However, the method was unsuccessful in eliminating the vortex rope structure. In fact, the pressure pulsations have increased with shape iterations. One possible reason for this is that the pressure pulsations and swirl are not directly linked. The main reason remains unchanged from the previous discussion: without eliminating the source of the vortex rope – the tangential velocity components – the structure will not be eliminated.

In the future, different adjoint solver software with a greater selection of objective functions can be employed to see whether different results can be obtained. Alternatively, a completely different algorithm for the shape optimization of the draft tube could be developed, as seen, for example, in the master's thesis of Oberta[39] (in Slovak).

In conclusion, the shape optimization of the draft tube is not effective when suppressing the vortex rope. In order to achieve this, it is necessary to suppress the source of the vortex rope. The geometric boundary condition, the shape of the draft tube and hub, has a minimal effect on the vortex rope behaviour. The most important boundary condition is the velocity profile at the diffuser inlet. This is also demonstrated in Oberta's work[39], where it can be seen that the shape optimization using a totally different algorithm has not resulted in suppressing the vortex rope.

Conclusion

The present work dealt with the computational shape optimization of a diffuser behind a swirl generator that mimics the runner of a Francis turbine. The optimization was based on the use of the adjoint solver in ANSYS Fluent. The main objective was to suppress the vortex rope in non-optimal regimes. A brief study on the vortex rope in water turbines was conducted. A large number of mitigation methods have been tested by researchers, yet they have been found to be only partially effective in suppressing the effects of the rotating vortex rope. In most cases, the mitigation of one effect leads to the amplification of another negative effect. Research on CFD simulations of the vortex rope indicates that the eddy viscosity models (k-ε, k-ω SST) are too dissipative and predict smaller vortex ropes. Therefore, more advanced models such as RSM or LES must be employed to reliably predict the vortex rope characteristics and behaviour.

The adjoint method, a mathematical tool for calculating gradients, was introduced. This method is effective in calculating gradients (sensitivities) for a large number of variables, such as coordinates of individual nodes of a computational mesh. This is the reason why the adjoint method proved effective for tasks involving the shape optimization, particularly in the automotive and aviation industry. The process for design iteration was presented, which involves calculating the flow field, finding the new shape using the adjoint solver, generating a new mesh, and calculating the flow field again.

Firstly, a shape optimization was conducted on a test case for a simple two-dimensional geometry in order to evaluate the capabilities and limitations of the adjoint solver and to establish a methodology for the adjoint shape optimization. Vortex shedding behind a cylinder was observed with the objective of minimizing drag. It showed that the presented iterative approach involving time-averaging of all flow variables is feasible. The objective function was successfully reduced by 63 %, showing that the adjoint solver can be effective for external shape optimization.

Three-dimensional, unsteady CFD simulations of the vortex rope inside the diffuser were carried out. A structured, hexahedral mesh was generated to ensure accurate results of the complex, swirling flow. RSM was selected for turbulence modelling due to its ability to perform well for highly swirling, anisotropic flows. Swirl around the diffuser axis was selected as the objective function for the adjoint solver to minimize. After six iterations, the diffuser transformed into a bell-shaped structure, with a narrow pipe section at the inlet and a wider section at the outlet, forming a bell shape. The shape of the hub remained almost unchanged. The newly generated mesh demonstrated high quality, with no discrepancies, even after multiple design iterations. The objective function was reduced by 18 %, suggesting a partial success of the adjoint optimization. However, the energy of the vortex rope was only transferred away from the hub, rather than suppressed, resulting in a narrower and longer vortex rope. The backflow region

has also only moved away from the hub but its size has not changed dramatically as a result of the shape optimization. The narrower cross sections lead to an overall increase of axial velocity inside the diffuser. The negative effects of the vortex rope, such as pressure pulsations, were not mitigated. Overall, the adjoint shape optimization was unsuccessful in suppressing the vortex rope.

When examining other research on the topic of vortex rope mitigation, specifically shape optimization of the diffuser, it was found that this approach was never successful in suppressing the vortex rope. This suggests that it is not an effective method, as the shape of the draft tube has minimal effect on the vortex rope behaviour. The solution lies in the manipulation of the velocity field, e.g. the velocity triangle at the runner outlet. Transforming the velocity triangle and thus reducing the tangential velocity component can be an effective solution. The Kaplan turbine, which is equipped with adjustable blades, is an effective solution to this problem. For the Francis turbine, a potential method for mitigating the vortex rope is through the use of active methods, which involve the injection of a fluid into the system.

References

1. KUMAR, Sandeep; CERVANTES, Michel J.; GANDHI, Bhupendra K. Rotating vortex rope formation and mitigation in draft tube of hydro turbines – A review from experimental perspective. *Renewable and Sustainable Energy Reviews*. 2021, vol. 136, p. 110354. ISSN 1364-0321. Available from DOI: 10.1016/j.rser.2020.110354.
2. RUDOLF, Pavel; LITERA, Jiří; ALEJANDRO IBARRA BOLANOS, Germán; ŠTEFAN, David. Manipulation of the swirling flow instability in hydraulic turbine diffuser by different methods of water injection. *EPJ Web Conf.* 2018, vol. 180, p. 02090. Available from DOI: 10.1051/epjconf/201817002090.
3. URBAN, Ondřej. *Reduced order model of the swirling flow*. Brno, 2022. Doctoral thesis. Brno University of Technology, Faculty of Mechanical Engineering. Supervised by Pavel RUDOLF. Available at https://www.vut.cz/studenti/zav-prace/detail/137904.
4. LEIBOVICH, Sidney. The Structure of Vortex Breakdown. *Annual Review of Fluid Mechanics*. 1978, vol. 10, no. 1, pp. 221–246. Available from DOI: 10.1146/annurev.fl.10.010178.001253.
5. FALER, J. H.; LEIBOVICH, Sidney. Disrupted states of vortex flow and vortex breakdown. *The Physics of Fluids*. 1977, vol. 20, no. 9, pp. 1385–1400. ISSN 0031-9171. Available from DOI: 10.1063/1.862033.
6. SARPKAYA, Turgut. On stationary and travelling vortex breakdowns. *Journal of Fluid Mechanics*. 1971, vol. 45, no. 3, pp. 545–559. Available from DOI: 10.1017/S0022112071000181.
7. NISHI, Michihiro; LIU, Shuhong. An Outlook on the Draft-Tube-Surge Study. *International Journal of Fluid Machinery and Systems*. 2013, vol. 6. Available from DOI: 10.5293/IJFMS.2013.6.1.033.
8. NISHI, Michihiro. Surging Characteristics of Conical and Elbow Type Draft Tubes. *Proc. 12th IAHR Symposium on Hydraulic Machinery and System, Stirling, 1984*. 1984, pp. 272–283. Available also from: https://cir.nii.ac.jp/crid/1573668926441225856.
9. HARVEY, John Kenneth. Some observations of the vortex breakdown phenomenon. *Journal of Fluid Mechanics*. 1962, vol. 14, no. 4, pp. 585–592. Available from DOI: 10.1017/S0022112062001470.
10. DÖRFLER, Peter; SICK, Mirjam; COUTU, A. *Flow-Induced Pulsation and Vibration in Hydroelectric Machinery: Engineer's Guidebook for Planning, Design and Troubleshooting*. Springer London, 2012. ISBN 9781447142522. Available from DOI: 10.1007/978-1-4471-4252-2.
11. RHEINGANS, W. Power Swings in Hydroelectric Power Plants. *Journal of Fluids Engineering*. 2023, vol. 62, pp. 171–177. Available from DOI: 10.1115/1.4021394.
12. NISHI, Michihiro; WANG, X. M.; YOSHIDA, K.; TAKAHASHI, T.; TSUKAMOTO, T. An Experimental Study on Fins, Their Role in Control of the Draft Tube Surging. In: *Hydraulic Machinery and Cavitation*. Dordrecht: Springer Netherlands, 1996, pp. 905–914. ISBN 978-94-010-9385-9.
13. DÖRFLER, Peter; LOHMBERG, A; MICHLER, W; SICK, Mirjam. Investigation of pressure pulsation and runner forces in a single-stage reversible pump turbine model. 2003, pp. 8–10.
14. VEKVE, Thomas. *An experimental investigation of draft tube flow*. Trondheim, 2004. Doctoral thesis. Norwegian University of Science and Technology.

15. LAUNDER, Brian; SPALDING, Dudley Brian. The Numerical Computation of Turbulent Flow Computer Methods. *Computer Methods in Applied Mechanics and Engineering*. 1974, vol. 3, pp. 269–289. ISBN 9780080309378. Available from DOI: 10.1016/0045-7825(74)90029-2.

16. VU, Thi; BERNARD, Nennemann; CIOCAN, Gabriel; SANDA, Iliescu; OLIVIER, Braun; AVELLAN, François. Experimental study and unsteady simulation of the Flindt draft tube rotating vortex rope. 2004, pp. 1–12.

17. SUSAN-RESIGA, Romeo; VU, Thi; MUNTEAN, Sebastian; CIOCAN, Gabriel; NENNEMANN, Bernd. Jet control of the draft tube vortex rope in Francis turbines at partial discharge. 2006, vol. 1, pp. 67–80.

18. RUPRECHT, Albert; HELMRICH, Thomas; ASCHENBRENNER, Thomas; SCHERER, Thomas. Simulation of vortex rope in a turbine draft tube. In: *Proceedings of the 21st IAHR Symposium on Hydraulic Machinery and Systems*. EPFL/STI/LMH, Lausanne, Switzerland, 2002, vol. 1, pp. 259–266.

19. YARAS, Metin; GROSVENOR, A. D. Evaluation of one- and two-equation low-Re turbulence models. Part I—Axisymmetric separating and swirling flows. *International Journal for Numerical Methods in Fluids*. 2003, vol. 42, no. 12, pp. 1293–1319. Available from DOI: 10.1002/fld.585.

20. MENTER, Florian. Two-equation eddy-viscosity turbulence models for engineering applications. *AIAA Journal*. 1994, vol. 32, no. 8, pp. 1598–1605. Available from DOI: 10.2514/3.12149.

21. SPALART, Philippe; ALLMARAS, Steven. A One-Equation Turbulence Model for Aerodynamic Flows. *AIAA*. 1992, vol. 439. Available from DOI: 10.2514/6.1992-439.

22. MINAKOV, Andrey; PLATONOV, Dmitriy; SENTYABOV, A.; GAVRILOV, Andrey. Francis-99 turbine numerical flow simulation of steady state operation using RANS and RANS/LES turbulence model. *Journal of Physics: Conference Series*. 2017, vol. 782. Available from DOI: 10.1088/1742-6596/782/1/012005.

23. RAJAN, Girish; CIMBALA, John. Computational and Theoretical Analyses of the Precessing Vortex Rope in a Simplified Draft Tube of a Scaled Model of a Francis Turbine. *Journal of Fluids Engineering*. 2016, vol. 139, no. 2. Available from DOI: 10.1115/1.4034693.

24. JUNGINGER, Bernd; RIEDELBAUCH, Stefan. Analysis of a full load operating point of a propeller turbine using scale-resolving turbulence models. *WASSERWIRTSCHAFT*. 2019, vol. 109, pp. 124–129. Available from DOI: 10.1007/s35147-019-0248-7.

25. FLEMMING, Felix; FOUST, J.; KOUTNIK, Jiri; FISHER, Richard. Overload Surge Investigation Using CFD Data. *International Journal of Fluid Machinery and Systems*. 2009, vol. 2. Available from DOI: 10.5293/IJFMS.2009.2.4.315.

26. KENWAY, Gaetan; MADER, Charles; HE, Ping; MARTINS, Joaquim. Effective Adjoint Approaches for Computational Fluid Dynamics. *Progress in Aerospace Sciences*. 2019. Available from DOI: 10.1016/j.paerosci.2019.05.002.

27. NEWMAN, James C.; TAYLOR, Arthur C.; BARNWELL, Richard W.; NEWMAN, Perry A.; HOU, Gene J.-W. Overview of sensitivity analysis and shape optimization for complex aerodynamic configurations. *Journal of Aircraft*. 1999, vol. 36, no. 1, pp. 87–96. Available from DOI: 10.2514/2.2416.

28. LIONS, Jacques Louis. *Optimal control of systems governed by partial differential equations*. Vol. 170. Springer, 1971. ISBN 978-3-642-65026-0.

29. PIRONNEAU, Olivier. On optimum design in fluid mechanics. *Journal of Fluid Mechanics*. 1974, vol. 64, no. 1, pp. 97–110. Available from DOI: 10.1017/S0022112074002023.

30. JAMESON, Antony. Aerodynamic Design via Control Theory. *Journal of Scientific Computing*. 1988, vol. 3. ISBN 978-3-540-50872-4. Available from DOI: 10.1007/BF01061285.

31. GILES, Mike; PIERCE, Niles. An Introduction to the Adjoint Approach to Design. *Flow, Turbulence and Combustion*. 2000, vol. 65. Available from DOI: 10.1023/A:1011430410075.

32. OTHMER, Carsten. Adjoint methods for car aerodynamics. *Journal of Mathematics in Industry*. 2014, vol. 4, p. 6. Available from DOI: 10.1186/2190-5983-4-6.

33. ANSYS, INC. *ANSYS Fluent User's Guide*. Release 2023 R2, 2023.

34. HAN, Taeyoung; HILL, Chris; JINDAL, Shailesh. Adjoint method for aerodynamic shape improvement in comparison with surface pressure gradient method. *SAE International Journal of Passenger Cars-Mechanical Systems*. 2011, vol. 4, no. 2011-01-0151, pp. 100–107. Available from DOI: 10.4271/2011-01-0151.

35. TZANAKIS, Athanasios. *Duct optimization using CFD software ANSYS Fluent Adjoint Solver*. Göteborg, 2014. PhD thesis. Chalmers University of Technology.

36. BUHMANN, M.D. *Radial Basis Functions: Theory and Implementations*. Cambridge University Press, 2003. Cambridge Monographs on Applied and Computational Mathematics. ISBN 9780521633383. Available also from: https://www.cambridge.org/cz/universitypress/subjects/mathematics/numerical-analysis/radial-basis-functions-theory-and-implementations.

37. NISHI, Michihiro; KUBOTA, Takashi; MATSUNAGA, Shigenori; SENOO, Yasutoshi. Study on swirl flow and surge in an elbow type draft tube. In: *Proc. IAHR 10th Symp., Tokyo, Japan*. 1980, vol. 1, pp. 557–568.

38. SUSAN-RESIGA, Romeo; MUNTEAN, Sebastian; BOSIOC, Alin; STUPARU, Adrian; MILOS, Teodor; BAYA, Alexandru; BERNAD, Sandor; ANTON, Liviu Eugen. Swirling flow apparatus and test rig for flow control in hydraulic turbines discharge cone. In: 2007, vol. 52, pp. 203–216. No. 66.

39. OBERTA, Brian. *Tvarová optimalizace sací trouby Francisovy turbíny pro potlačení vírového copu*. Brno, 2023. Master's thesis. Brno University of Technology, Faculty of Mechanical Engineering. Available at https://www.vut.cz/studenti/zav-prace/detail/150378.

List of Symbols and Abbreviations

Symbols

Symbol	Unit	Description
$\mathbf{c}$	$-$	adjoint sensitivity vector
c_p	1	pressure coefficient
D_h	m	hydraulic diameter
f	$-$	function of interest
F_d	N	drag force
F_L	N	lift force
g	$\mathrm{m} \cdot \mathrm{s}^{-2}$	gravitational acceleration
I	1	turbulent intensity
k	$\mathrm{m}^2 \cdot \mathrm{s}^{-2}$	turbulent kinetic energy
K	1	cavitation number
m	1	swirl rate
NPSH	m	net positive suction head
ΔP	W	total power loss
p	Pa	gauge pressure
Q	$\mathrm{m}^3 \cdot \mathrm{s}^{-1}$	volumetric flow rate
Q_{ax}	$\mathrm{m}^3 \cdot \mathrm{s}^{-1}$	flow rate from axial inlet of the generator
Q_{tan}	$\mathrm{m}^3 \cdot \mathrm{s}^{-1}$	flow rate from tangential inlet of the generator
r	m	radial distance
R	m	radius of the draft tube
$\mathbf{R}$	$-$	vector of residuals for the governing equations
S	m^2	area
Sr	$\mathrm{kg} \cdot \mathrm{m}^2 \cdot \mathrm{s}^{-1}$	swirl

Symbol	Unit	Description
u	$\mathrm{m} \cdot \mathrm{s}^{-1}$	circumferential velocity
u_τ	$\mathrm{m} \cdot \mathrm{s}^{-1}$	friction velocity at the nearest wall
v	$\mathrm{m} \cdot \mathrm{s}^{-1}$	absolute velocity
v_{ij}	s^{-1}	strain rate tensor
v_m	$\mathrm{m} \cdot \mathrm{s}^{-1}$	axial component of the absolute velocity
v_u	$\mathrm{m} \cdot \mathrm{s}^{-1}$	tangential component of the absolute velocity
w	$\mathrm{m} \cdot \mathrm{s}^{-1}$	relative velocity
y	m	distance to the nearest wall
y^+	1	dimensionless wall distance
$\mathbf{w}$	$-$	vector of state variables
$\mathbf{x}$	$-$	vector of design variables
α	1	Coriolis number
ε	$\mathrm{m}^2 \cdot \mathrm{s}^{-3}$	turbulence eddy dissipation
μ	$\mathrm{Pa} \cdot \mathrm{s}$	dynamic viscosity
ν	$\mathrm{m}^2 \cdot \mathrm{s}^{-1}$	kinematic viscosity
ρ	$\mathrm{kg} \cdot \mathrm{m}^{-3}$	density
ϕ	rad	swirl angle
ψ	$-$	adjoint vector
ω	s^{-1}	turbulence eddy frequency
σ	$\mathrm{W} \cdot \mathrm{m}^{-3}$	dissipation function

Abbreviations

Abbreviation	Description
ANSYS	Analysis System
BEP	Best Efficiency Point
CFD	Computational Fluid Dynamics
DES	Detached-Eddy Simulation
HL	High Load
LES	Large-Eddy Simulation
PDE	Partial Differential Equation
PL	Part Load
PRESTO!	Pressure Staggering Option
QUICK	Quadratic Upstream Interpolation for Convective Kinematics
RANS	Reynolds Average Navier-Stokes
RSM	Reynolds Stress Model
SAS	Scale Adaptive Simulation
SBES	Stress-Blended Eddy Simulation
SIMPLE	Semi-Implicit Method for Pressure Linked Equations
SST	Shear Stress Transport
URANS	Unsteady Reynolds-Averaged Navier-Stokes

List of Figures

List of Tables